1 **Boundary of nighttime ozone chemical equilibrium in the mesopause region: long-**

2 **term evolution determined using 20-year satellite observations**

3 Mikhail Yu. Kulikov[1], Mikhail V. Belikovich[1], Aleksey G. Chubarov[1], Svetlana O. Dementyeva[1], and

4 Alexander M. Feigin[1]

5 [1]A. V. Gaponov-Grekhov Institute of Applied Physics of the Russian Academy of Sciences, 46 Ulyanov

6 Str., 603950 Nizhny Novgorod, Russia

7 Correspondence to: Mikhail Yu. Kulikov (mikhail_kulikov@mail.ru)

Abstract. The assumption of nighttime ozone chemical equilibrium (NOCE) is widely employed for retrieving the O_x-HO_x components in the mesopause from rocket and satellite measurements. In this work, the recently developed analytical criterion of determining the NOCE boundary is used (i) to study the connection of this boundary with O and H spatiotemporal variability based on 3D modeling of chemical transport, and (ii) to retrieve and analyze the spatiotemporal evolution of the NOCE boundary in 2002-2021 from the SABER/TIMED data set. It was revealed, first, that the NOCE boundary reproduces well the transition zone dividing deep and weak photochemical oscillations of O and H caused by the diurnal variations of solar radiation. Second, the NOCE boundary is sensitive to sporadic abrupt changes in the middle atmosphere dynamics, in particular, due to powerful sudden stratospheric warmings leading to the events of an elevated (up to ~80 km) stratopause, which took place in January-March 2004, 2006, 2009, 2010, 2012, 2013, 2018, and 2019. Third, the space-time evolution of this characteristic expressed via pressure altitude contains a clear signal of 11-year solar cycle in the 55ºS-55ºN range. In particular, the mean annual NOCE boundary averaged in this range of latitudes anticorrelates well with $F_{10.7}$ index with the coefficient -0.95. Moreover, it shows a weak linear trend of the 56.2±42.2 m/decade.

1 Introduction

The mesopause (80-100 km) is an interesting region of the Earth's atmosphere possessing quite a number of unique phenomena and processes which can be considered as sensitive indicators/predictors of global climate change and anthropogenic influences on atmospheric composition (e.g., Thomas et al., 1989). Here, the summer temperature at middle and high latitudes reaches its lowest values (down to 100K (Schmidlin, 1992)). The temperatures below 150K lead to water vapour condensation and formation of the highest altitude clouds in the Earth's atmosphere, the so-called Polar Mesospheric Clouds or Noctilucent Clouds consisting primarily of water ice (Thomas, 1991). In turn, the temperature of the winter mesopause is essentially higher, so there is a strong negative temperature gradient between the summer and winter hemispheres. At these altitudes, atmospheric waves of various spatiotemporal scales are observed, in particular, internal gravity waves coming from the lower atmosphere. Destruction of gravity waves leads to strong turbulence that affects the atmospheric circulation and ultimately manifests itself in the mentioned temperature structure of this region.

Many layer phenomena in the mesopause are related to the photochemistry of the O_x-HO_x components (O, O_3, H, OH, and HO_2). There is a narrow (in height) transition region where photochemistry behaviour transforms rapidly from "deep" diurnal oscillations, when the difference between daytime and nighttime values of the O_x-HO_x components can reach several orders of magnitude, to weak photochemical oscillations. As a result, above this region, O and H accumulate to form the

corresponding layers. This layer formation manifests itself in the appearance of a secondary ozone maximum and airglow layers of OH and O excited states. Thus, O_x-HO_x photochemistry in the mesopause is responsible for the presence of important (first of all, from a practical point of view) indicators observed in the visible and infrared ranges, which are widely used for ground-based and satellite monitoring of climate changes and wave activity. Moreover, O_x-HO_x photochemistry provides the total chemical heating rate of this region, influences the radiative cooling and other useful airglows (for example, by O_2 excited states), is involved in the plasma-chemical reactions and formation of layers of the ionosphere. The mentioned transformation of O_x-HO_x behaviour with height may occur via the nonlinear response of O_x-HO_x photochemistry to the diurnal variations of solar radiation in the form of subharmonic (with periods of 2, 3, 4, and more days) or chaotic oscillations (e.g., Sonnemann and Fichtelmann, 1997; Feigin et al., 1998). This unique phenomenon was predicted many years ago (Sonnemann and Fichtelmann, 1987) and investigated theoretically by models taking into account different transport processes (Sonnemann and Feigin, 1999; Sonnemann et al., 1999; Sonnemann and Grygalashvyly, 2005; Kulikov and Feigin, 2005; Kulikov, 2007; Kulikov et al., 2020). It was revealed, in particular, that the nonlinear response is controlled by vertical eddy diffusion (Sonnemann and Feigin, 1999; Sonnemann et al., 1999), so that 2-day oscillations can only survive at real diffusion coefficients, but the eddy diffusion in zonal direction leads to the appearance of the so-called reaction-diffusion waves in the form of propagating phase fronts of 2-day oscillations (Kulikov and Feigin, 2005; Kulikov et al., 2020). Recently, the satellite data processing revealed the first evidence of the existence of 2-day photochemical oscillations in the real mesopause (Kulikov et al., 2021).

While regular remote sensing measurements of most O_x-HO_x components are still limited, the indirect methods based on the physicochemical assumptions are useful tools for monitoring these trace gases. In many papers, O and H distributions were retrieved from the daytime and nighttime rocket and satellite measurements of the ozone and the volume emission rates of OH(v), O(^{1}S), and O_2(a$^1\Delta_g$) (Good, 1976; Pendleton et al., 1983; McDade et al., 1985; McDade and Llewellyn, 1988; Evans et al., 1988; Thomas, 1990; Llewellyn et al., 1993; Llewellyn and McDade, 1996; Mlynczak et al., 2007, 2013a, 2013b, 2014, 2018; Smith et al., 2010; Xu et al., 2012; Siskind et al., 2008, 2015). The retrieval technique is based on the assumption of ozone photochemical/chemical equilibrium and physicochemical model of the corresponding airglow, which describe the relationship between local O and H values and measurement data.

The daytime photochemical ozone equilibrium is a good approximation everywhere in the mesosphere – lower thermosphere (MLT) region (Kulikov et al., 2017) due to ozone photodissociation, whereas the applicability of the assumption of nighttime ozone chemical equilibrium (NOCE) is limited: there is an altitude boundary above which NOCE is satisfied to an accuracy better than 10%. Below this

boundary, the ozone equilibrium is disturbed essentially and cannot be used. Good (1976) supposed that NOCE is fulfilled above 60 km, whereas other papers apply the NOCE starting from 80 km, independent of latitude and season. However, studies of NOCE within the framework of the 3D chemical-transport models (Belikovich et al., 2018; Kulikov et al., 2018a) revealed that the NOCE boundary varies within the range of 81–87 km, depending on latitude and season. In view of the practical need to determine the local altitude position of this boundary, Kulikov et al. (2018a) presented a simple criterion determining the equilibrium boundary using only the data provided by the SABER (Sounding of the Atmosphere using Broadband Emission Radiometry) instrument onboard the TIMED (Thermosphere Ionosphere Mesosphere Energetics and Dynamics). Making use of this criterion, Kulikov et al. (2019) retrieved the annual evolution of the NOCE boundary from the SABER data. It was revealed that a two-month averaged NOCE boundary essentially depends on season and latitude and can rise up to ~ 86 km. Moreover, the analysis of the NOCE boundary in 2003-2005 showed that this characteristic was sensitive to unusual dynamics of stratospheric polar vortex during the 2004 Arctic winter, which was named a remarkable winter in the 50-year record of meteorological analyses (Manney et al., 2005). Moreover, Belikovich et al. (2018) found by 3D simulation that the excited OH layer repeats well spatiotemporal variability of the NOCE boundary. These results allowed us to speculate that the NOCE boundary can be considered as an important indicator of mesopause processes.

The main goals of this paper are (1) to investigate the relationship between the NOCE boundary according to the mentioned criterion and O and H variability with the use of the 3D chemical transport model, and (2) to retrieve and analyze the spatiotemporal evolution of the NOCE boundary in 2002-2021 from the SABER/TIMED data set. In the next section, we present the used model. In Section 3, we briefly describe the criterion of determining the NOCE boundary local height and study how this height is related to the features of O and H distributions from the 3D model. Section 4 explains the methodology of determining the NOCE boundary from satellite data. Section 5 presents the main results obtained from SABER/TIMED data discussed in Section 6.

2 3D model

We use the 3D chemical transport model of the middle atmosphere developed by the Leibniz Institute of Atmospheric Physics (Sonnemann et al., 1998; Körner and Sonnemann, 2001; Grygalashvyly et al., 2009; Hartogh et al., 2004, 2011). The three-dimensional fields of temperature and winds were adopted by Kulikov et al. (2018b) from the Canadian Middle Atmosphere Model (Scinocca et al., 2008) for the year 2000 with an updated frequency of 6 hours. To exclude unrealistic jumps in the evolution of calculated chemical characteristics, linear smoothing between two subsequent updates of these parameters

is applied. The model takes into account 3D advective transport and vertical diffusive transport (both, turbulent and molecular). The Walcek-scheme (Walcek, 2000) and the implicit Thomas algorithm (Morton and Mayers, 1994) are used for advective and diffusive transport, respectively. The model grid includes 118 pressure-height levels (from the ground to ~135 km), 32 and 64 levels in latitude and longitude, respectively. The chemical part considers 22 constituents (O, O(^{1}D), O_3, H, OH, HO_2, H_2O_2, H_2O, N, NO, NO_2, NO_3, N_2O, CH_4, CH_2, CH_3, CH_3O_2, CH_3O, CH_2O, CHO, CO, CO_2), 54 two- and three-body reactions, and 15 photo-dissociation reactions. The model uses pre-calculated dependences of dissociation rates on altitude and solar zenith angle (Kremp et al., 1999). The chemistry is calculated by the Shimazaki scheme (Shimazaki, 1985) for the integration time of 9 sec.

3 The NOCE criterion

The nighttime ozone chemistry at the mesopause heights is determined mainly by two reactions R1-R2 (e.g., Allen et al., 1984), see Table 1. The secondary ozone loss via the $O + O_3 \rightarrow 2O_2$ reaction becomes important above ~ 95 km (Smith et al., 2009). Kulikov et al. (2023) verified with simulated and measured data that this reaction does not influence the NOCE boundary determination and may be skipped. Thus, the ozone equilibrium concentration ($O_3{}^{eq}$) corresponding to the instantaneous balance between the production and loss terms is as follows:

$$O_3{}^{eq} = \frac{k_1 \cdot O \cdot O_2 \cdot M}{k_2 \cdot H}, \tag{1}$$

where M is air concentration, and k_{1-2} are the corresponding rate constants of the reactions (see Table 1).

As mentioned above, the NOCE criterion was developed in Kulikov et al. (2018a). The main idea is that the local values of O_3 and $O_3{}^{eq}$ are close ($O_3(t) \approx O_3{}^{eq}(t)$), when $\tau_{O_3} \ll \tau_{O_3}{}^{eq}$, where τ_{O_3} is the ozone lifetime and $\tau_{O_3}{}^{eq}$ is the local time scale of $O_3{}^{eq}$:

$$\tau_{O_3} = \frac{1}{k_2 \cdot H}, \tag{2}$$

$$\tau_{O_3}{}^{eq} \equiv \frac{O_3{}^{eq}}{|dO_3{}^{eq}/dt|} = \frac{O}{H \cdot \left|\frac{d}{dt}\left(\frac{O}{H}\right)\right|}. \tag{3}$$

As shown in Kulikov et al. (2018a), $\tau_{O_3}{}^{eq}$ can be determined from a simplified photochemical model describing the O_x-HO_x evolution in the mesopause region (Feigin et al., 1998), so the criterion of the NOCE validity can be written in the form:

$$Cr = \frac{\tau_{O_3}}{\tau_{O_3}{}^{eq}} = 2\frac{k_1 \cdot k_4 \cdot O_2{}^2 \cdot M^2}{k_2}\left(1 - \frac{k_5 + k_6}{k_3}\right) \cdot \frac{1}{k_2 \cdot H \cdot O_3} \ll 1, \tag{4}$$

137 where k_i are the corresponding reaction constants from Table 1. Calculations with the global 3D

138 chemistry-transport model of the middle atmosphere showed (Kulikov et al. 2018a) that the criterion

139 $\tau_{O_3}/\tau_{O_3}{}^{eq} \leq 0.1$ defines well the boundary of the area where $|O_3/O_3{}^{eq} - 1| \leq 0.1$.

140   Kulikov et al. (2023) presented the theory of chemical equilibrium of a certain trace gas n. Strictly

141 mathematically, the cascade of sufficient conditions for $n_i(t) \cong n_i{}^{eq}(t)$ was derived considering its

142 lifetime, equilibrium concentration, and time dependences of these characteristics. In case of the

143 nighttime ozone, it was proved that $\tau_{O_3}/\tau_{O_3}{}^{eq} \ll 1$ is the main condition for NOCE validity and the

144 criterion $\tau_{O_3}/\tau_{O_3}{}^{eq} \leq 0.1$ limits a possible difference between O_3 and $O_3{}^{eq}$ to not more than ~10%.

145 Moreover, Kulikov et al. (2023) slightly corrected the expression for the criterion (4):

146 $$\text{Cr} = 2 \frac{k_1 \cdot O_2 \cdot M}{k_2} \left(k_4 \cdot M \cdot O_2 \cdot \left(1 - \frac{k_5 + k_6}{k_3} \right) + k_2 \cdot O_3 \right) \cdot \frac{1}{k_2 \cdot H \cdot O_3} \leq 0.1. \tag{5}$$

147 One more important condition for $O_3 \approx O_3{}^{eq}$ at the time moment t is:

148 $$e^{\int_{t_{bn}}^{t} \tau_{O_3}{}^{-1} dt} \gg 1, \tag{6}$$

149 where t_{bn} is the time of the beginning of the night. The ozone equilibrium concentration jumps at sunset

150 due to the shutdown of photodissociation. Thus, the condition (6) shows that it takes time for the ozone

151 concentration to reach a new equilibrium. Kulikov et al. (2023) revealed that, at the solar zenith angle $\chi >$

152 95°, the condition (6) is fulfilled almost in all cases and the condition (5) becomes the main criterion for

153 NOCE validity. In addition, Kulikov et al. (2023) demonstrated with the use of a 3-D model that the

154 criterion (5) almost ideally reproduces the NOCE boundary found by direct comparison of O_3 and $O_3{}^{eq}$

155 concentrations, see Figure 1 in Kulikov et al. (2023).

156   Figures 1-3 demonstrate model examples of O and H time-height variations above different points

157 over three months. In order to focus attention on diurnal oscillations, the concentrations are normalized by

158 mean daily values, which were calculated as a function of altitude. These daily average O and H values

159 were different for each altitude. One can see in all panels of these figures "deep" diurnal oscillations that

160 occur below 81-87 km. Due to the shutdown of sources at night and high rates of the main HO_x and O

161 sinks nonlinearly dependent on air concentration (Konovalov and Feigin, 2000), the variables change

162 during each night within the range of several orders of magnitude with low values of time evolution.

163 Above 83-88 km, the situation differs essentially from the previous case. One can see relatively weak

164 diurnal oscillations. These regimes of O and H behaviour are consistent, i.e. deep H diurnal oscillations

165 correspond to the same dynamics in O, and so on. There exists a few-km thick layer (transition zone)

166 dividing deep and weak oscillations whose height position depends on latitude and season. In particular,

167 in summer the middle latitude transition is higher than in winter. Figures 1-3 show also the magenta lines

168 pointing the NOCE boundary in accordance with the criterion (5) ($\text{Cr} = 0.1$). One can see that the NOCE

criterion almost perfectly reproduces the features of the transition zone. Thus, our criterion is not only a useful technical characteristic to retrieve O from satellite data, but it also points to an important dynamical process in the O_x-HO_x photochemistry.

4 NOCE boundary from satellite data

We use version 2.0 of the SABER data product (Level2A) for the simultaneously measured profiles of pressure (p), altitude (z), temperature (T), O_3 (at 9.6 μm), and total volume emission rates of OH* transitions at 2.0 (VER) within the 0.0001–0.02 mbar pressure interval (altitudes approximately 75–105 km) in 2002-2021. We consider only nighttime data when the solar zenith angle $\chi > 95°$.

Kulikov et al. (2018a) noted that the term $k_2 \cdot H \cdot O_3$ in the expression for the NOCE criterion can be rewritten in the form depending on measurable characteristics only with the use of the corresponding OH(v) model by Mlynczak et al. (2013a):

$$k_2 \cdot H \cdot O_3 = VER/A(T,M,O), \tag{7}$$

where $A(T,M,O)$ is the function in square brackets in Eq. (3) in the paper by Mlynczak et al. (2013a) with the parameters corrected by Mlynczak et al. (2018):

$$A(T,M,O) =$$

$$\frac{0.47 \cdot 118.35}{215.05 + 2.5 \cdot 10^{-11} \cdot O_2 + 3.36 \cdot 10^{-13} \cdot e^{\frac{220}{T}} \cdot N_2 + 3 \cdot 10^{-10} \cdot O} + \frac{0.34 \cdot 117.21}{178.06 + 4.8 \cdot 10^{-13} \cdot O_2 + 7 \cdot 10^{-13} \cdot N_2 + 1.5 \cdot 10^{-10} \cdot O} +$$

$$\frac{0.47 \cdot 117.21 \cdot (20.05 + 4.2 \cdot 10^{-12} \cdot O_2 + 4 \cdot 10^{-13} \cdot N_2)}{(215.05 + 2.5 \cdot 10^{-11} \cdot O_2 + 3.36 \cdot 10^{-13} \cdot e^{\frac{220}{T}} \cdot N_2 + 3 \cdot 10^{-10} \cdot O) \cdot (178.06 + 4.8 \cdot 10^{-13} \cdot O_2 + 7 \cdot 10^{-13} \cdot N_2 + 1.5 \cdot 10^{-10} \cdot O)}. \tag{8}$$

This function is the result of the combination of the equations of physicochemical OH* balance in the $v = 8$ and $v = 9$ states. It depends on the constants of the processes describing sources and sinks at the corresponding levels, in particular, the OH(v) removal on collisions with O_2, N_2, and O. Below 86-87 km, $A(T,M,O) \cong A(T,M,O=0) \equiv A(T,M)$ due to relativity small O concentrations. Thus, by combining Eqs. (5) and (7), the NOCE criterion for SABER data can be recast in the following form:

$$VER \geq VER_{min}(T,M) = 20 \cdot \frac{k_1 \cdot O_2 \cdot M}{k_2} \left(k_4 \cdot O_2 \cdot M \cdot \left(1 - \frac{k_5 + k_6}{k_3} \right) + k_2 \cdot O_3 \right) \cdot A(T,M). \tag{9}$$

Due to the strong air-concentration dependence VER_{min} decreases rapidly with height. In particular, at 105 km, $VER \gg VER_{min}$. At 75 km, the relationship is inverse. We determine the local position of the NOCE boundary (pressure level $p_{eq}{}^l$ and altitude level $z_{eq}{}^l$) according to the criterion (9), where $VER = VER_{min}(T,M)$. We verified that the approximation $A(T,M,O) \cong A(T,M)$ is valid near the NOCE boundary. With the use of annual SABER data, we calculated simultaneous datasets of $A(T,M)$

198 and $A(T, M, O)$. In the second case, we used O retrieved from the same SABER data. The maximum and

199 mean differences between $A(T, M)$ and $A(T, M, O)$ were found to be ~ 2% and ~ 0.1%, respectively.

200   The total range of latitudes according to the satellite trajectory over a month was ~(83.5°S - 83.5°N).

201 This range was divided into 20 bins and all local values of $p_{eq}{}^{l}$ and $z_{eq}{}^{l}$ falling into one bin during a

202 month or a year were averaged, respectively. In particular, several thousand values of $p_{eq}{}^{l}$ and $z_{eq}{}^{l}$ fall

203 into one bin during a month. Following Mlynczak et al. (2013a), averages were determined by binning

204 the data of a certain day by local hour and then averaging over the hour bins that contain data to obtain

205 the daily average value. Then we calculated monthly mean values of $p_{eq}{}^{m}$ and $z_{eq}{}^{m}$ and annually mean

206 values of $p_{eq}{}^{y}$ and $z_{eq}{}^{y}$ (hereafter, the indexes «m» and «y» indicate the monthly and annually average,

207 respectively). Then, for convenience, the values of $p_{eq}{}^{m}$ and $p_{eq}{}^{y}$ were recalculated into the pressure

208 altitudes $h_{eq}{}^{m}$ and $h_{eq}{}^{y}$. The dependence of $h_{eq}{}^{m,y}$ on $p_{eq}{}^{m,y}$ was adopted from Mlynczak et al. (2013a,

209 2014):

210 $$h_{eq}{}^{m,y} = -H_a \cdot \log\left(p_{eq}{}^{m,y}/p_0\right), H_a = 5.753474, p_0 = 11430.49428 \text{ hPa}. \qquad (10)$$

211 Note that the use of both, geometrical and pressure coordinates is a rather common approach when

212 analyzing long-term evolution of the obtained data, especially, when the data is the result of averaging

213 over time and space. In particular, Lübken et al. (2013) demonstrated the importance of distinguishing

214 between trends on pressure and geometrical altitudes in the mesosphere, since the second includes the

215 atmospheric shrinking effect and is more pronounced. Grygalashvyly et al. (2014) analyzed the linear

216 trends in OH* peak height and revealed a remarkable decrease at geometrical altitudes, which is almost

217 absent at pressure altitudes.

218   Kulikov et al. (2023) studied the systematic uncertainty of the retrieved NOCE boundary height.

219 Following the typical analysis presented, for example, in Mlynczak et al. (2013a, 2014), the uncertainty

220 was obtained by calculating the root-sum-square of the individual sensitivity of the retrieved

221 characteristic to the perturbation of O_3, T, rates of reactions, and parameters of the A function. The

222 systematic error of NOCE pressure altitude $h_{eq}{}^{m}$ and geometrical altitude $z_{eq}{}^{m}$ varied in the range of

223 0.1-0.3 km, whereas the random error was negligible due to averaging over time and space.

224

225 **5 NOCE boundary in 2002-2021 from SABER/TIMED data: main results**

226   Figure 4 demonstrates the time evolution of the pressure altitude $h_{eq}{}^{m}$ in 2002-2021 in all latitude

227 bins. Figures 5 (left column) show the mean (for 2002-2021) annual cycle of $h_{eq}{}^{m}$ at four specific

228 latitudes and Figures 6 (left column) present the Fourier spectra at these latitudes obtained from the data

in Figure 4. Note, first, that above ~58ºS,N, there are data gaps specified by the satellite sensing geometry. For example, in 2002-2014, at 66.8-75.15°S,N measurements covered 6 months per year only. In 2015, because of slight changes in the satellite geometry, there appeared additional months. This is especially noticeable above ~66ºS,N and manifests itself by extension of the variation range of $h_{eq}{}^m$ at these latitudes in 2015-2021. Second, the variation range of $h_{eq}{}^m$, annual cycle and spectrum of harmonic oscillations depends essentially on the latitude. Near the equator, $h_{eq}{}^m$ varies in the 81-83 km range mainly and there are two main harmonics with periods of 1/2 and 1 year in the spectrum. At low latitudes, the variation range of $h_{eq}{}^m$ narrows down to a minimum (~82-83 km at 16.7-20.05°S,N), which is accompanied with the appearance of a wide spectrum of harmonics with periods of 1/5, 1/4, 1/3, 1/2, and 1 year. At middle latitudes, the range of $h_{eq}{}^m$ variation monotonically increases up to ~81.5-85.5 km with latitude and the harmonic with a period of 1 year becomes the main mode in the spectrum of oscillations. At both, low and middle latitudes, there is no signal from quasi-biennial oscillations but one can see a remarkable amplitude of a harmonic with a period of ~10 years, which can be associated with a manifestation of 11-year solar cycle. It is interesting that the mentioned features are typical for both hemispheres. At high latitudes, $h_{eq}{}^m$ varies in the range of 79-86.5 km. At these latitudes, one can see the main difference between the northern and southern hemispheres: the sharp falls and rises of the northern boundary of NOCE by several km (up to 3-4 km) appearing in January-March 2004, 2006, 2009, 2010, 2012, 2013, 2018 and 2019 that are absent at southern latitudes.

The analysis of Figures 5-6 demonstrates the following redistribution in the annual cycle with increasing latitude from equator to polar latitudes. Near the equator, the annual cycle has two maxima in June – July and in December – January. The first one is more pronounced. That is why there are two main harmonics with periods of 1/2 and 1 year in the spectrum. At low latitudes, one maximum (summer) does not change, while the other approaches the first one. As a result, the spectrum of harmonics is wide. At middle latitudes, the maxima gradually merge so that the 1 year-harmonic becomes the main one.

Figure 7 (left) demonstrates a contour map of the space-time evolution of the average annual pressure altitude $h_{eq}{}^y$ in 2002-2021. Figure 8 presents the time evolution of this characteristic at different latitudes. Based on the Fourier spectra presented in Figures 6 (left column), we can suppose that, at low and middle latitudes, the interannual variation of $h_{eq}{}^y$ is caused by the 11-year solar cycle mainly. Figure 9 (left) presents the correlation coefficient of $h_{eq}{}^y$ with $F_{10.7}$ index (solar radio flux at 10.7 cm, see the red curve in Figure 10) as a function of latitude. One can see good anticorrelation (with a coefficient from -0.72 to -0.92) between ~55ºS and ~55ºN. At high latitudes, the absolute value of the correlation coefficient decreases sharply down to ~0.58 in the south and to ~0.1 in the north. The blue curve in Figure

261   10 shows latitude-averaged $h_{eq}{}^y$ in the range of 55ºS-55ºN. In this case, the anticorrelation with $F_{10.7}$

262   index is close to ideal (coefficient ~ -0.95).

263   With the use of multiple linear regression in the 55ºS-55ºN range:

264    $$h_{eq}{}^y(year) = const + \alpha \cdot year + \beta \cdot F_{10.7}(year), \qquad\qquad (11)$$

265   we determined a slow (up to 10 m/year) linear trend of $h_{eq}{}^y$ as a function of latitude, but with the

266   uncertainties essentially larger than the trend values. Applying the regression analysis to latitude-averaged

267    $h_{eq}{}^y$ (blue curve in Figure 10) gave us a more statistically significant value of the trend: 5.62±4.22

268   m/year.

269   Figure 11 demonstrates the time evolution of the geometrical altitude $z_{eq}{}^m$ in 2002-2021 in all

270   latitude bins. Figures 5 (right column) show the mean (for 2002-2021) annual cycle of $z_{eq}{}^m$ at four

271   specific latitudes and Figures 6 (right column) present the Fourier spectra at these latitudes obtained from

272   the data in Figure 11. Comparison with Figures 4 and 5-6 (left columns) shows that $z_{eq}{}^m$ repeats many

273   qualitative features of the space-time evolution of pressure altitude $h_{eq}{}^m$. In particular, in the direction

274   from the equator to the poles, the variation range of $z_{eq}{}^m$ first decreases down to 1 km at 16º-25ºS,N and

275   then expands to several km at middle and high latitudes. One can see the same redistribution of the annual

276   cycle with latitude, similarly to the pressure altitude case. Near the equator, the annual cycle possesses

277   two maxima occurring in June – July and in December – January. At low latitudes, one maximum

278   continues in summer, whereas the other shifts to spring. At middle latitudes, the maxima gradually

279   coalesce forming a single summer maximum. At high northern latitudes, there are the same local sharp

280   variations of the NOCE boundary in January-February 2004, 2006, 2009, 2010, 2012, 2013, 2018 and

281   2019, which are absent at southern latitudes. One can see from Figure 5 that, on the average, $z_{eq}{}^m$ is

282   lower than $h_{eq}{}^m$ by 0.5-1 km, depending on latitude. One can see from Figure 6 that the $z_{eq}{}^m$ spectra of

283   harmonic oscillations are similar to the $h_{eq}{}^m$ spectra except for the absence of a signal of the 11-year

284   solar cycle.

285   Figure 7(right) demonstrates a contour map of space-time evolution of the annually average

286   geometrical altitude $z_{eq}{}^y$ in 2002-2021. Figure 12 presents the time evolution of this characteristic at

287   different latitudes. One can see that there is no clear evidence of 11-year solar cycle manifestation at all

288   latitudes. This is confirmed by the calculation of the correlation coefficient of $z_{eq}{}^y$ with $F_{10.7}$ index as a

289   function of latitude (see Figure 9 (right)). Moreover, the latitude-averaged (in the range of 55ºS-55ºN)

290    $z_{eq}{}^y$ has a correlation coefficient equal to ~-0.55.

291   As in the case of $h_{eq}{}^y$, we found with the use of multiple linear regression the slow (up to ~-10

292   m/year) and statistically insignificant linear trend of $z_{eq}{}^y$ as a function of latitude. Moreover, the

293   regression analysis of latitude-averaged $z_{eq}{}^y$ also revealed a statistically insignificant trend.

294

295   **6 Discussion**

296   The NOCE boundary is an important technical characteristic for correct application of the NOCE

297   approximation to retrieve the nighttime distributions of minor chemical species of MLT. Kulikov et al.

298   (2019) repeated the O and H retrieval by Mlynczak et al. (2018) from the SABER data for the year 2004.

299   It was revealed that the application of the NOCE condition below the boundary obtained according to the

300   criterion could lead to a great (up to 5–8 times) systematic underestimation of O concentration below 86

301   km, whereas it was insignificant for H retrieval. The results presented in Figures 4, 5 and 11 demonstrate

302   that, except for high northern latitudes, there is a stable annual cycle of the NOCE boundary. The monthly

303   mean boundary can rise up to geometrical altitudes of 82-83 km (~$(5.2\text{-}6.2)\cdot10^{-3}$ hPa) at low latitudes and

304   up to 84-85 km (~$(3.7\text{-}4.4)\cdot10^{-3}$ hPa) at middle and high latitudes. Thus, the SABER O data below these

305   altitudes/pressures may be essentially incorrect and the retrieval approaches without using the NOCE

306   condition (e.g., Panka et al., 2018) should be more appropriate.

307   Note that the NOCE condition was used not only for O and H derivation from satellite data. This

308   assumption is a useful approach helping (i) to study hydroxyl emission in the MLT region with simulated

309   and measured data, in particular, OH* mechanisms, morphology and variability caused, for example, by

310   atmospheric tides and gravity wave activity (e.g., Marsh et al., 2006; Nikoukar et al., 2007; Xu et al.,

311   2010, 2012; Kowalewski et al., 2014; Sonnemann et al., 2015); (ii) to analyze the MLT response to

312   sudden stratospheric warmings (SSWs) (e.g., Smith et al., 2009); (iii) to derive exothermic heating rates

313   of MLT (e.g., Mlynczak et al., 2013b); (iv) to analytically simulate the mesospheric OH* layer response

314   to gravity waves (e.g., Swenson and Gardner, 1998); and (v) to derive the analytical dependence of

315   excited hydroxyl layer number density and peak altitude on atomic oxygen and temperature (e.g.,

316   Grygalashvyly et al., 2014; Grygalashvyly, 2015). Perhaps some results require revision or reanalysis

317   taking the NOCE boundary into account. For example, Smith et al. (2009) used the NOCE condition to

318   analyze the ozone perturbation in the MLT, in particular, during the SSW at the beginning of 2009 (the

319   central day was January 24). Our preliminary results of processing the SABER and simulated data in

320   January 2009 show that the NOCE boundary above 70ºN may jump from ~80 km to ~90-95 km due to a

321   short-time abrupt temperature fall above 80 km during this SSW. Thus, one can assume that the NOCE

322   condition is not a good approximation for the description of ozone variations directly in the process of

323 SSWs. This case will be studied in a separate work. Note also that after the SSW of January 2009 there
324 began a long-time (several tens of days) event of elevated (up to ~80-85 km) stratopause (see, e.g., Figure
325 1 in Smith et al. (2009)), which led to the corresponding increase of temperature above 80 km. The
326 occurrence of this event and its duration are in a good correlation with sharp lowering of the NOCE
327 boundary at high northern latitudes (see Figures 4 and 11). Moreover, all abrupt changes of the NOCE
328 boundary at these latitudes in January-March of other years (2004, 2006, 2010, 2012, 2013, 2018, and
329 2019) can be also associated with the elevated stratopause events in these years (see García-Comas et al.
330 (2020) and references there).

331 According to the used chemical-transport model, the NOCE boundary reproduces well the transition
332 zone dividing deep and weak diurnal oscillations of O and H (see Figures 1-3). We verified this feature
333 with the annual run of SD-WACCM-X model for the year 2017 provided by the NCAR High Altitude
334 Observatory (https://doi.org/10.26024/5b58-nc53). Despite the low time resolution of the downloaded
335 data (3-hour averaging), we obtained the results (see Figure 13) similar to Figures 1-3. Note also that both
336 models give the same consistence between the altitudes of the NOCE boundary and the mentioned
337 transition zone at high latitudes in spring and autumn.

338 The space-time evolution of the NOCE boundary expressed in terms of pressure altitudes contains a
339 clear signal of the 11-year solar cycle in the 55ºS-55ºN range, which is suppressed mainly at high
340 latitudes. The weak correlation of $h_{eq}{}^{y}$ with $F_{10.7}$ index at high southern latitudes may be caused by the
341 mentioned data gaps specified by the satellite sensing geometry. The same reason and distortions by
342 SSWs evidently determine no correlation at high northern latitudes. Thus, at low and middle latitudes
343 $h_{eq}{}^{y}$ can be considered as a sensitive indicator of solar activity. Below, we present a simple and short
344 explanation for this. Let us consider the NOCE criterion (9) at the pressure level p_{eq}:

$$VER(p_{eq}) = VER_{min}\left(T, M(p_{eq})\right).$$

345 In a zero approximation

346 $$VER_{min} = 20 \cdot \frac{k_1 \cdot O_2(p_{eq}) \cdot M(p_{eq}) \cdot \left(k_4 \cdot O_2(p_{eq}) \cdot M(p_{eq}) \cdot \left(1 - \frac{k_5 + k_6}{k_3}\right) + k_2 \cdot O_3(p_{eq})\right) \cdot A\left(T, M(p_{eq})\right)}{k_2} \cong$$

347 $$20 \cdot \frac{k_1 \cdot k_4 \cdot (O_2(p_{eq}) \cdot M(p_{eq}))^2 \cdot A\left(T, M(p_{eq})\right)}{k_2} \sim \frac{k_1 \cdot k_4 \cdot (p_{eq}/T)^4 \cdot A(T, p_{eq})}{k_2} \sim \frac{exp(470/T) \cdot p_{eq}{}^4 \cdot A(T, p_{eq})}{T^{8.2}},$$

348 where $A(T, p_{eq}) =$

349 $$\frac{0.47 \cdot 118.35}{215.05 + 2.5 \cdot 10^{-11} \cdot O_2 / M \cdot \frac{p_{eq}}{k_B T} + 3.36 \cdot 10^{-13} \cdot e^{\frac{220}{T}} \cdot N_2 / M \cdot \frac{p_{eq}}{k_B T}} + \frac{0.34 \cdot 117.21}{178.06 + 4.8 \cdot 10^{-13} \cdot O_2 / M \cdot \frac{p_{eq}}{k_B T} + 7 \cdot 10^{-13} \cdot N_2 / M \cdot \frac{p_{eq}}{k_B T}} +$$

350 $$\frac{0.47 \cdot 117.21 \cdot (20.05 + 4.2 \cdot 10^{-12} \cdot O_2 / M \cdot \frac{p_{eq}}{k_B T} + 4 \cdot 10^{-13} \cdot N_2 / M \cdot \frac{p_{eq}}{k_B T})}{(215.05 + 2.5 \cdot 10^{-11} \cdot O_2 / M \frac{p_{eq}}{k_B T} + 3.36 \cdot 10^{-13} \cdot e^{\frac{220}{T}} \cdot N_2 / M \frac{p_{eq}}{k_B T}) \cdot (178.06 + 4.8 \cdot 10^{-13} \cdot O_2 / M \cdot \frac{p_{eq}}{k_B T} + 7 \cdot 10^{-13} \cdot N_2 / M \cdot \frac{p_{eq}}{k_B T})}.$$

351 Our analysis of $A(T, p_{eq})$ shows that this function can be approximately rewritten as $A(T, p_{eq}) \approx$

352 $const + \frac{const}{const + \frac{p_{eq}}{T}}$. So, one can see that VER_{min} is strongly dependent on T. Moreover, it anticorrelates

353 with T. Gan et al. (2017) and Zhao et al. (2020) analyzed the simulated and measured data and revealed a

354 clear correlation between the MLT temperature above 80 km and the 10.7-cm solar radio flux. Moreover,

355 the dependence of the correlation coefficient of T with $F_{10.7}$ index on latitude in the 55ºS-55ºN range

356 given in Figure 9 in the paper by of Zhao et al. (2020) is consistent with our Figure 9 (left panel), taking

357 into account the sign of the correlation. Thus, we can conclude that the found anticorrelation of the NOCE

358 boundary $h_{eq}{}^y$ with solar activity is caused by the strong connection with temperature, which, in turn, is

359 in a good correlation with the $F_{10.7}$ index. A detailed analysis of the reasons why the solar cycle weakly

360 manifests itself in the spatio-temporal variability of $z_{eq}{}^y$ is not so simple and is beyond the scope of this

361 work.

362 Figure 5 illustrates an interesting peculiarity. At middle latitudes, the summer $h_{eq}{}^m$ and $z_{eq}{}^m$ are

363 remarkably (by several kilometers) higher than the winter ones, while the opposite relationship could be

364 expected. Due to more effective daytime HO_x photoproduction at these altitudes, the summer H values at

365 the beginning of the night are higher than the ones in winter. So, the summer ozone lifetimes should be

366 shorter and the NOCE condition is more favourable than in winter. Nevertheless, the same ratio between

367 the summer and winter NOCE boundaries at middle latitudes was revealed in Belikovich et al. (2018) and

368 Kulikov et al. (2018a), where the boundary of this equilibrium was determined by direct comparison of

369 O_3 and $O_3{}^{eq}$ concentrations from results of 3D chemical-transport models. Based on the results of Section

370 3, we can assume that the discussed effect is connected with the height position of the transition zone,

371 which demonstrates the same variation (see Figures 1-3). Kulikov et al. (2023) derived the equations

372 describing pure chemical O and H nighttime evolution:

373 $$\begin{cases} \frac{dO}{dt} = -2 \cdot k_4 \cdot M \cdot O_2 \cdot H - 2 \cdot k_2 \cdot H \cdot O_3 \\ \frac{dH}{dt} = -2 \cdot k_4 \cdot M \cdot O_2 \cdot \frac{k_5 + k_6}{k_3} \cdot \frac{H^2}{O} \end{cases} . \tag{12}$$

374 Neglecting the second term in the first equation as a secondary one, this system can be solved

375 analytically, so that the nighttime evolution times of O and H are:

$$376 \quad \tau_O \equiv \frac{O}{|dO/dt|} = \frac{1}{2 \cdot k_4 \cdot M \cdot O_2} \cdot \left(\frac{O}{H}\right)_{t=t_{bn}} - \left(1 - \frac{k_5 + k_6}{k_3}\right) \cdot (t - t_{bn}), \qquad (13)$$

$$377 \quad \tau_H \equiv \frac{H}{|dH/dt|} = \frac{1}{2 \cdot k_4 \cdot M \cdot O_2} \cdot \frac{k_3}{k_5 + k_6} \cdot \left(\frac{O}{H}\right)_{t=t_{bn}} - \left(\frac{k_3}{k_5 + k_6} - 1\right) \cdot (t - t_{bn}), \qquad (14)$$

378 where t_{bn} is the time of the beginning of the night, $\left(\frac{O}{H}\right)_{t=t_{bn}}$ is the O/H ratio at the beginning of the

379 night. Note that k_3 is much larger than $k_5 + k_6$ (see Table 1). Based on the daytime O and H distributions

380 in the mesopause region obtained in Kulikov et al. (2022), we calculated the ratio of the summer O/H to

381 the winter O/H (see Figure 14). During the summer, O/H at middle latitudes is remarkably less than in

382 winter in both, northern and southern hemispheres, whereas the air concentration and the rate of reaction

383 R4 (see Table 1) increase due to a decrease in temperature. As a result, the summer τ_O and τ_H are

384 essentially shorter than their winter values, which explains the summer rise of the transition zone and the

385 NOCE boundary.

386   Finally, let us briefly discuss other qualitative indicators of the NOCE boundary, which could be

387 found in the SABER database. As mentioned above, Kulikov et al. (2019) showed that the nighttime O

388 SABER profiles are correct above the NOCE boundary, whereas the H profiles hold within the whole

389 pressure interval. Kulikov et al. (2021) demonstrated that, in the altitude range of 80-85 km, many H

390 profiles have a sharp jump in concentration when it increases from ~ 10^7 cm^{-3} to ~ 10^8 cm^{-3}. Our analysis

391 with the criterion (9) shows that the altitude of these jumps can be used as a rough indicator of the NOCE

392 boundary.

393

7 Conclusions

395   The NOCE criterion is not only a useful technical characteristic for the retrieval of O from satellite

396 data, but it also reproduces the transition zone position which separates deep and weak diurnal

397 oscillations of O and H at low and middle latitudes. At middle latitudes, the summer boundary of NOCE

398 is remarkably (by several kilometers) higher than the winter one, which is accompanied with the same

399 variation of the transition zone. This effect is explained by the markedly lower values of the O and H

400 nighttime evolution times in summer than in winter by virtue of the lower values of the O/H ratio at the

401 beginning of the night and air concentration increase.

402   The NOCE boundary according to the criterion is sensitive to sporadic abrupt changes in the

403 dynamics of the middle atmosphere.

404   The NOCE boundary at low and middle latitudes expressed in pressure altitudes contains a clear

405 signal of 11-year solar cycle and can be considered as a sensitive indicator of solar activity.

406

Data availability. The SABER data are obtained from the website (https://saber.gats-inc.com). The data of solar radio flux at 10.7 cm in 2002-2021 were downloaded from http://www.wdcb.ru/stp/solar/solar_flux.ru.html and https://www.spaceweather.gc.ca/forecast-prevision/solar-solaire/solarflux/sx-5-en.php.

411

Code availability. Code is available upon request.

413

Author contributions. MK and MB performed data processing and analysis and wrote the manuscript. AC, SD, and AM contributed to reviewing the article.

416

Competing interests. The authors declare that they have no conflict of interest.

418

Acknowledgements. The authors are grateful to the SABER team for data availability.

420

Financial support. The main results presented in Section 5 were obtained under the support by the Russian Science Foundation under grant No. 22-12-00064 (https://rscf.ru/project/22-12-00064/). The analysis of the difference between the NOCE boundary in summer and winter at middle latitudes and the reasons of well anticorrelation of the NOCE boundary with $F_{10.7}$ index were carried out at the expense of state assignment no. 0729-2020-0037.

426

References

Allen, M., Lunine, J. I., and Yung, Y. L.: The vertical distribution of ozone in the mesosphere and lower thermosphere, J. Geophys. Res., 89(D3), 4841–4872, https://doi.org/10.1029/JD089iD03p04841, 1984.

Belikovich, M. V., Kulikov, M. Yu, Grygalashvyly, M., Sonnemann, G. R., Ermakova, T. S., Nechaev, A. A., and Feigin, A .M.: Ozone chemical equilibrium in the extended mesopause under the nighttime conditions, Adv. Space Res., 61, 426–432, https://doi.org/10.1016/j.asr.2017.10.010, 2018.

Burkholder, J. B., Sander, S. P., Abbatt, J., Barker, J. R., Cappa, C., Crounse, J. D., Dibble, T. S., Huie, R. E., Kolb, C. E., Kurylo, M. J., Orkin, V. L., Percival, C. J., Wilmouth, D. M., and Wine, P. H.:

Chemical Kinetics and Photochemical Data for Use in Atmospheric Studies, Evaluation No. 19, JPL Publication 19-5, Jet Propulsion Laboratory, Pasadena, http://jpldataeval.jpl.nasa.gov, 2020.

Evans, W. F. J., McDade, I. C., Yuen, J., and Llewellyn, E. J.: A rocket measurement of the O_2 infrared atmospheric (0-0) band emission in the dayglow and a determination of the mesospheric ozone and atomic oxygen densities, Can. J. Phys., 66, 941–946, https://doi.org/10.1139/p88-151. 1988.

Gan, Q., Du, J., Fomichev, V. I., Ward, W. E., Beagley, S. R., Zhang, S., and Yue, J.: Temperature responses to the 11 year solar cycle in the mesosphere from the 31 year (1979–2010) extended Canadian Middle Atmosphere Model simulations and a comparison with the 14 year (2002–2015) TIMED/SABER observations, J. Geophys. Res. Space Physics, 122, 4801–4818, https://doi.org/10.1002/2016JA023564, 2017.

García-Comas, M., Funke, B., López-Puertas, M., González-Galindo, F., Kiefer, M., and Höpfner, M.: First detection of a brief mesoscale elevated stratopause in very early winter. Geophys. Res. Lett., 47, e2019GL086751, https://doi.org/10.1029/2019GL086751, 2020.

Good, R. E.: Determination of atomic oxygen density from rocket borne measurements of hydroxyl airglow, Planet. Space Sci., 24, 389–395, https://doi.org/10.1016/0032-0633(76)90052-0, 1976.

Grygalashvyly, M., Sonnemann, G. R., and Hartogh, P.: Long-term behavior of the concentration of the minor constituents in the mesosphere - A model study, Atmos. Chem. Phys., 9, 2779–2792, https://doi.org/10.5194/acp-9-2779-2009, 2009.

Grygalashvyly, M., Sonnemann, G. R., Lübken, F.-J., Hartogh, P., and Berger, U.: Hydroxyl layer: Mean state and trends at midlatitudes, J. Geophys. Res. Atmos., 119, 12,391–12,419, https://doi.org/10.1002/2014JD022094, 2014.

Grygalashvyly, M.: Several notes on the OH* layer, Ann. Geophys., 33, 923-930, https://doi.org/10.5194/angeo-33-923-2015, 2015.

Hartogh, P., Jarchow, C., Sonnemann, G. R., and Grygalashvyly, M.: On the spatiotemporal behavior of ozone within the upper mesosphere/mesopause region under nearly polar night conditions, J. Geophys. Res., 109, D18303, https://doi.org/10.1029/2004JD004576, 2004.

Hartogh, P., Jarchow, Ch., Sonnemann, G. R., and Grygalashvyly, M.: Ozone distribution in the middle latitude mesosphere as derived from microwave measurements at Lindau (51.66°N, 10.13°E), J. Geophys. Res., 116, D04305, https://doi.org/10.1029/2010JD014393, 2011.

Feigin, A. M., Konovalov, I. B., and Molkov, Y. I.: Towards understanding nonlinear nature of atmospheric photochemistry: Essential dynamic model of the mesospheric photochemical system., J. Geophys. Res.: Atmos., 103, 25,447–25,460, https://doi.org/10.1029/98JD01569, 1998.

Konovalov, I. B., and Feigin, A. M.: Towards an understanding of the non-linear nature of atmospheric photochemistry: origin of the complicated dynamic behavior of the mesospheric photochemical system, Nonlin. Processes Geophys., 87-104, https://doi.org/10.5194/npg-7-87-2000, 2000.

Körner, U., and Sonnemann, G. R.: Global 3D-modeling of water vapor concentration of the mesosphere/mesopause region and implications with respect to the NLC region, J. Geophys. Res., 106, 9639– 9651, https://doi.org/10.1029/2000JD900744, 2001.

Kowalewski, S., v. Savigny, C., Palm, M., McDade, I. C., and Notholt, J.: On the impact of the temporal variability of the collisional quenching process on the mesospheric OH emission layer: a study based on SD-WACCM4 and SABER, Atmos. Chem. Phys., 14, 10193-10210, https://doi.org/10.5194/acp-14-10193-2014, 2014.

Kremp, C., Berger, U., Hoffmann, P., Keuer, D., and Sonnemann, G. R.: Seasonal variation of middle latitude wind fields of the mesopause region—A comparison between observation and model calculation, Geophys. Res. Lett., 26, 1279–1282, https://doi.org/10.1029/1999GL900218, 1999.

Kulikov, M. Yu., and Feigin, A. M.: Reactive-diffusion waves in the mesospheric photochemical system. Adv. Space Res., 35(11), 1992-1998, https://doi.org/10.1016/j.asr.2005.04.020, 2005.

Kulikov, M. Yu.: Theoretical investigation of the influence of a quasi 2-day wave on nonlinear photochemical oscillations in the mesopause region, J. Geophys. Res., 112, D02305, https://doi.org/10.1029/2005JD006845, 2007.

Kulikov, M. Y., Belikovich, M. V., Grygalashvyly, M., Sonnemann, G. R., Ermakova, T. S., Nechaev, A. A., and Feigin, A. M.: Daytime ozone loss term in the mesopause region, Ann. Geophys., 35, 677-682 https://doi.org/10.5194/angeo-35-677-2017, 2017.

Kulikov, M. Y., Belikovich, M. V., Grygalashvyly, M., Sonnemann, G. R., Ermakova, T. S., Nechaev, A. A., and Feigin, A. M.: Nighttime ozone chemical equilibrium in the mesopause region. J. Geophys. Res.,123, 3228–3242, https://doi.org/10.1002/2017JD026717, 2018a.

Kulikov, M. Y., Nechaev, A. A., Belikovich, M. V., Ermakova, T. S., and Feigin, A. M.: Technical note: Evaluation of the simultaneous measurements of mesospheric OH, HO_2, and O_3 under a photochemical equilibrium assumption – a statistical approach, Atm. Chem. Phys., 18, 7453-747, https://doi.org/10.5194/acp-18-7453-2018, 2018b.

Kulikov, M. Yu., Nechaev, A. A., Belikovich, M. V., Vorobeva, E. V., Grygalashvyly, M., Sonnemann, G. R., and Feigin, A. M.: Border of nighttime ozone chemical equilibrium in the mesopause region from saber data: implications for derivation of atomic oxygen and atomic hydrogen, Geophys. Res. Lett., 46, 997– 1004, https://doi.org/10.1029/2018GL080364, 2019.

Kulikov, M. Y., Belikovich, M. V., and Feigin, A. M.: Analytical investigation of the reaction-diffusion waves in the mesopause photochemistry, J. Geophys. Res., 125, e2020JD033480, https://doi.org/10.1029/2020JD033480, 2020.

Kulikov, M. Y., Belikovich, M. V., Feigin, A. M.: The 2-day photochemical oscillations in the mesopause region: the first experimental evidence? Geophys. Res. Lett., 48, e2021GL092795, https://doi.org/10.1029/2021GL092795, 2021.

Kulikov, M. Y., Belikovich, M. V., Grygalashvyly, M., Sonnemann, G. R., and Feigin, A.M.: The revised method for retrieving daytime distributions of atomic oxygen and odd-hydrogens in the mesopause region from satellite observations, Earth Planets Space, 74, 44, https://doi.org/10.1186/s40623-022-01603-8, 2022.

Kulikov, M. Yu., Belikovich, M. V., Chubarov, A. G., Dementeyva, S. O., Feigin, A. M.: Boundary of nighttime ozone chemical equilibrium in the mesopause region: improved criterion of determining the boundary from satellite data, Adv. Space Res., 71 (6), 2770-2780, https://doi.org/10.1016/j.asr.2022.11.005, 2023.

Llewellyn, E. J., McDade, I. C. Moorhouse, P. and Lockerbie M. D.: Possible reference models for atomic oxygen in the terrestrial atmosphere, Adv. Space Res., 13, 135–144, https://doi.org/10.1016/0273-1177(93)90013-2, 1993.

Llewellyn, E. J., and McDade, I. C.: A reference model for atomic oxygen in the terrestrial atmosphere, Adv. Space Res., 18, 209–226, https://doi.org/10.1016/0273-1177(96)00059-2, 1996.

Lübken, F.-J., Berger, U. and Baumgarten, G.: Temperature trends in the midlatitude summer mesosphere, J. Geophys. Res. Atmos., 118, 13347–13360, https://doi.org/10.1002/2013JD020576, 2013.

Manney, G. L., Kruger, K., Sabutis, J. L., Sena, S. A., and Pawson, S.: The remarkable 2003–2004 winter and other recent warm winters in the Arctic stratosphere since the late 1990s. J. Geophys. Res., 110, D04107, https://doi.org/10.1029/2004JD005367, 2005.

Marsh, D. R., Smith, A. K., Mlynczak, M. G., and Russell III, J. M.: SABER observations of the OH Meinel airglow variability near the mesopause, J. Geophys. Res., 111, A10S05, https://doi.org/10.1029/2005JA011451, 2006.

McDade, I. C., Llewellyn, E. J., and Harris, F. R.: Atomic oxygen concentrations in the lower auroral thermosphere, Adv. Space Res., 5, 229–232, https://doi.org/10.1029/GL011I003P00247, 1985.

McDade, I. C., and Llewellyn, E. J.: Mesospheric oxygen atom densities inferred from night-time OH Meinel band emission rates, Planet. Space Sci., 36, 897–905, https://doi.org/10.1016/0032-0633(88)90097-9, 1988.

Mlynczak, M. G., Marshall, B. T., Martin-Torres, F. J., Russell III, J. M., Thompson, R. E., Remsberg, E. E., and Gordley, L. L.: Sounding of the Atmosphere using Broadband Emission Radiometry observations of daytime mesospheric $O_2(^1D)$ 1.27 μm emission and derivation of ozone, atomic oxygen, and solar and chemical energy deposition rates, J. Geophys. Res., 112, D15306, https://doi.org/10.1029/2006JD008355, 2007.

Mlynczak, M. G., Hunt, L. A., Mast, J. C., Marshall, B. T., Russell III, J. M., Smith, A. K., Siskind, D. E., Yee, J.-H., Mertens, C. J., Martin-Torres, F. J., Thompson, R. E., Drob, D. P., and Gordley, L. L.: Atomic oxygen in the mesosphere and lower thermosphere derived from SABER: Algorithm theoretical basis and measurement uncertainty, J. Geophys. Res., 118, 5724–5735, https://doi.org/10.1002/jgrd.50401, 2013a.

Mlynczak, M. G., Hunt, L. H., Mertens, C. J., Marshall, B. T., Russell III, J. M., López-Puertas, M., Smith, A. K., Siskind, D. E., Mast, J. C., Thompson, R. E., and Gordley, L. L.: Radiative and energetic constraints on the global annual mean atomic oxygen concentration in the mesopause region, J. Geophys. Res. Atmos., 118, 5796–5802, https://doi.org/10.1002/jgrd.50400, 2013b.

Mlynczak, M. G., Hunt, L. A. Marshall, B. T. Mertens, C. J. Marsh, D. R. Smith, A. K. Russell, J. M. Siskind D. E., and Gordley L. L.: Atomic hydrogen in the mesopause region derived from SABER: Algorithm theoretical basis, measurement uncertainty, and results, J. Geophys. Res., 119, 3516–3526, https://doi.org/10.1002/2013JD021263, 2014.

Mlynczak, M. G., Hunt, L. A., Russell, J. M. III, and Marshall, B. T.: Updated SABER night atomic oxygen and implications for SABER ozone and atomic hydrogen, Geophys. Res. Lett., 45, 5735–5741, https://doi.org/10.1029/2018GL077377, 2018.

Morton, K. W., and Mayers, D. F.; Numerical Solution of Partial Differential Equations, Cambridge University Press, 1994.

Nikoukar, R., Swenson, G. R., Liu, A. Z., and Kamalabadi, F.: On the variability of mesospheric OH emission profiles, J. Geophys. Res., 112, D19109, https://doi.org/10.1029/2007JD008601, 2007.

Panka, P. A., Kutepov, A. A., Rezac, L., Kalogerakis, K. S., Feofilov, A. G., Marsh, D., Janches, D., and Yiğit, E. Atomic oxygen retrieved from the SABER 2.0- and 1.6-μ m radiances using new first-principles nighttime OH(v) model, Geophys. Res. Lett., 45, 5798–5803, https://doi.org/10.1029/2018GL077677, 2018.

Pendleton, W. R., Baker, K. D., Howlett, L. C.: Rocket-based investigations of O(^{3}P), O$_2$ (a$^1\Delta_g$) and OH* (v=1,2) during the solar eclipse of 26 February 1979, J. Atm. Terr. Phys., 45(7), 479-491, 1983.

Siskind, D. E., Marsh, D. R., Mlynczak, M. G., Martin-Torres, F. J., and Russell III, J. M.: Decreases in atomic hydrogen over the summer pole: Evidence for dehydration from polar mesospheric clouds? Geophys. Res. Lett., 35, L13809, https://doi.org/10.1029/2008GL033742, 2008.

Siskind, D. E., Mlynczak, M. G., Marshall, T., Friedrich, M., Gumbel, J.: Implications of odd oxygen observations by the TIMED/SABER instrument for lower D region ionospheric modeling, J. Atmos. Sol. Terr. Phys., 124, 63–70, https://doi.org/10.1016/j.jastp.2015.01.014, 2015.

Schmidlin, F .J.: First observation of mesopause temperature lower than 100 K, Geophys. Res. Lett., 19, 1643-1646, https://doi.org/10.1029/92GL01506, 1992.

Shimazaki, T.: Minor Constituents in the Middle Atmosphere, D. Reidel, Norwell, Mass., USA, 444 pp., 1985.

Smith, A. K., Lopez-Puertas, M., Garcıa-Comas, M. and Tukiainen, S.: SABER observations of mesospheric ozone during NH late winter 2002–2009, Geophys. Res. Lett., 36, L23804, https://doi.org/10.1029/2009GL040942, 2009.

Smith, A. K., Marsh, D. R. Mlynczak, M. G. and Mast, J. C.: Temporal variations of atomic oxygen in the upper mesosphere from SABER, J. Geophys. Res., 115, D18309, https://doi.org/10.1029/2009JD013434, 2010.

Sonnemann, G., and Fichtelmann, B.: Enforced oscillations and resonances due to internal non-linear processes of photochemical system in the atmosphere, Acta. Geod. Geophys. Mont. Hung., 22, 301–311, 1987.

Sonnemann, G., and Fichtelmann, B.: Subharmonics, cascades of period of doubling and chaotic behavior of photochemistry of the mesopause region, J. Geophys. Res., 101, 1193-1203, https://doi.org/10.1029/96JD02740, 1997.

Sonnemann, G., Kremp, C. Ebel, A. and Berger U.: A three-dimensional dynamic model of minor constituents of the mesosphere, Atmos. Environ., 32, 3157–3172, https://doi.org/10.1016/S1352-2310(98)00113-7, 1998.

Sonnemann, G., Feigin, A. M., and Molkov, Ya. I.: On the influence of diffusion upon the nonlinear behaviour of the photochemistry of the mesopause region, J. Geophys. Res., 104, 30591-30603, https://doi.org/10.1029/1999JD900785, 1999.

Sonnemann, G., and Feigin, A. M.: Non-linear behaviour of a reaction-diffusion system of the photochemistry within the mesopause region, Phys. Rev. E, 59, 1719-1726, https://doi.org/10.1103/PhysRevE.59.1719, 1999.

Sonnemann, G. R.: The photochemical effects of dynamically induced variations in solar insolation, J. Atmos. Sol. Terr. Phys., 63, 781-797, https://doi.org/10.1016/S1364-6826(01)00010-4, 2001.

Sonnemann, G. R., and Grygalashvyly, M.: On the two-day oscillations and the day-to-day variability in global 3-D-modeling of the chemical system of the upper mesosphere/mesopause region, Nonlin. Processes Geophys., 12, 691– 705, https://doi.org/10.5194/npg-12-691-2005, 2005.

Sonnemann, G. R., Hartogh, P., Berger, U., and Grygalashvyly, M.: Hydroxyl layer: trend of number density and intra-annual variability, Ann. Geophys., 33, 749–767, https://doi.org/10.5194/angeo-33-749-2015, 2015.

Swenson, G. R., and Gardner C. S.: Analytical models for the responses of the mesospheric OH* and Na layers to atmospheric gravity waves, J. Geophys. Res., 103(D6), 6271–6294, https://doi.org/10.1029/97JD02985, 1998.

Thomas, G. E., Olivero, J. J., Jensen, E. J., Schroder, W., and Toon, O. B.: Relation between increasing methane and the presence of ice clouds at the mesopause, Nature, 338, 490–492https://doi.org/10.1038/338490a0, 1989.

Thomas, R. J.: Atomic hydrogen and atomic oxygen density in the mesosphere region: Global and seasonal variations deduced from Solar Mesosphere Explorer near-infrared emissions, J. Geophys. Res., 95, 16,457–16,476, https://doi. org/ 10. 1029/ JD095 iD10p 16457, 1990.

Thomas, G. E.: Mesospheric clouds and the physics of the mesopause region, Rev. Geophys., 29, 553–575, https://doi.org/10.1029/91RG01604, 1991.

Walcek, C. J.: Minor flux adjustment near mixing ratio extremes for simplified yet highly accurate monotonic calculation of tracer advection, J. Geophys. Res., 105, 9335-9348, https://doi.org/10.1029/1999JD901142, 2000.

Xu, J., Smith, A. K., Jiang, G., Gao, H., Wei, Y., Mlynczak, M. G., and Russell III, J. M.: Strong longitudinal variations in the OH nightglow, Geophys. Res. Lett., 37, L21801, https://doi.org/10.1029/2010GL043972, 2010.

Xu, J., Gao, H. Smith, A. K. and Zhu Y.: Using TIMED/SABER nightglow observations to investigate hydroxyl emission mechanisms in the mesopause region, J. Geophys. Res., 117, D02301, https://doi.org/10.1029/2011JD016342, 2012.

Zhao, X. R., Sheng, Z. Shi, H. Q. Weng, L. B. and He Y.: Middle Atmosphere Temperature Changes Derived from SABER Observations during 2002–20, J. Climate, 34, 7995–8012, https://doi.org/10.1175/JCLI-D-20-1010.1, 2021.

623 **Table 1.** List of reactions with corresponding reaction rates (for three-body reactions [cm^6 molecule^{-2}
624 s^{-1}], for two-body reactions [cm^3 molecule^{-1} s^{-1}]) taken from Burkholder et al. (2020).

	Reaction	Rate constant
R1	$O+O_2+M \rightarrow O_3+M$	$k_1 = 6.1 \cdot 10^{-34}(298/T)^{2.4}$
R2	$H+O_3 \rightarrow O_2+OH$	$k_2 = 1.4 \cdot 10^{-10}exp(-470/T)$
R3	$O+HO_2 \rightarrow O_2+OH$	$k_3 = 3 \cdot 10^{-11}exp(200/T)$
R4	$H+O_2+ M \rightarrow HO_2+M$	$k_4 = 5.3 \cdot 10^{-32}(298/T)^{1.8}$
R5	$H+HO_2 \rightarrow O_2+H_2$	$k_5 = 6.9 \cdot 10^{-12}$
R6	$H+HO_2 \rightarrow O+H_2O$	$k_6 = 1.6 \cdot 10^{-12}$

625

626

627
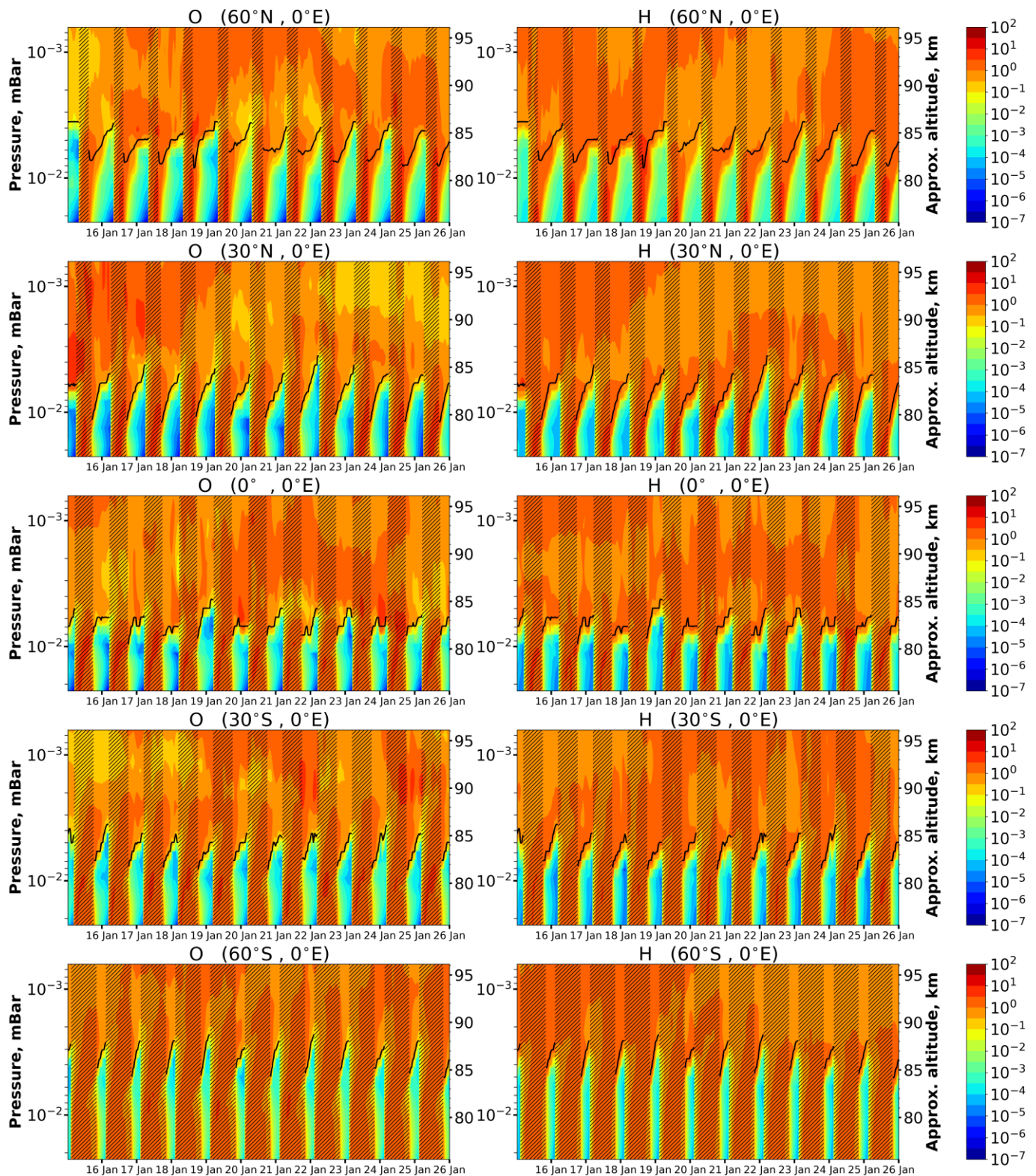
Figure 1. O and H time-height variations above different points in January 2000 calculated by 3D chemical transport model of middle atmosphere. Concentrations are normalized by mean daily values, correspondingly, calculated as a function of altitude. Dark bars mark daytime, light bars mark nighttime. Black lines point the NOCE boundary altitude in accordance to criterion (5) (Cr = 0.1).

632

633
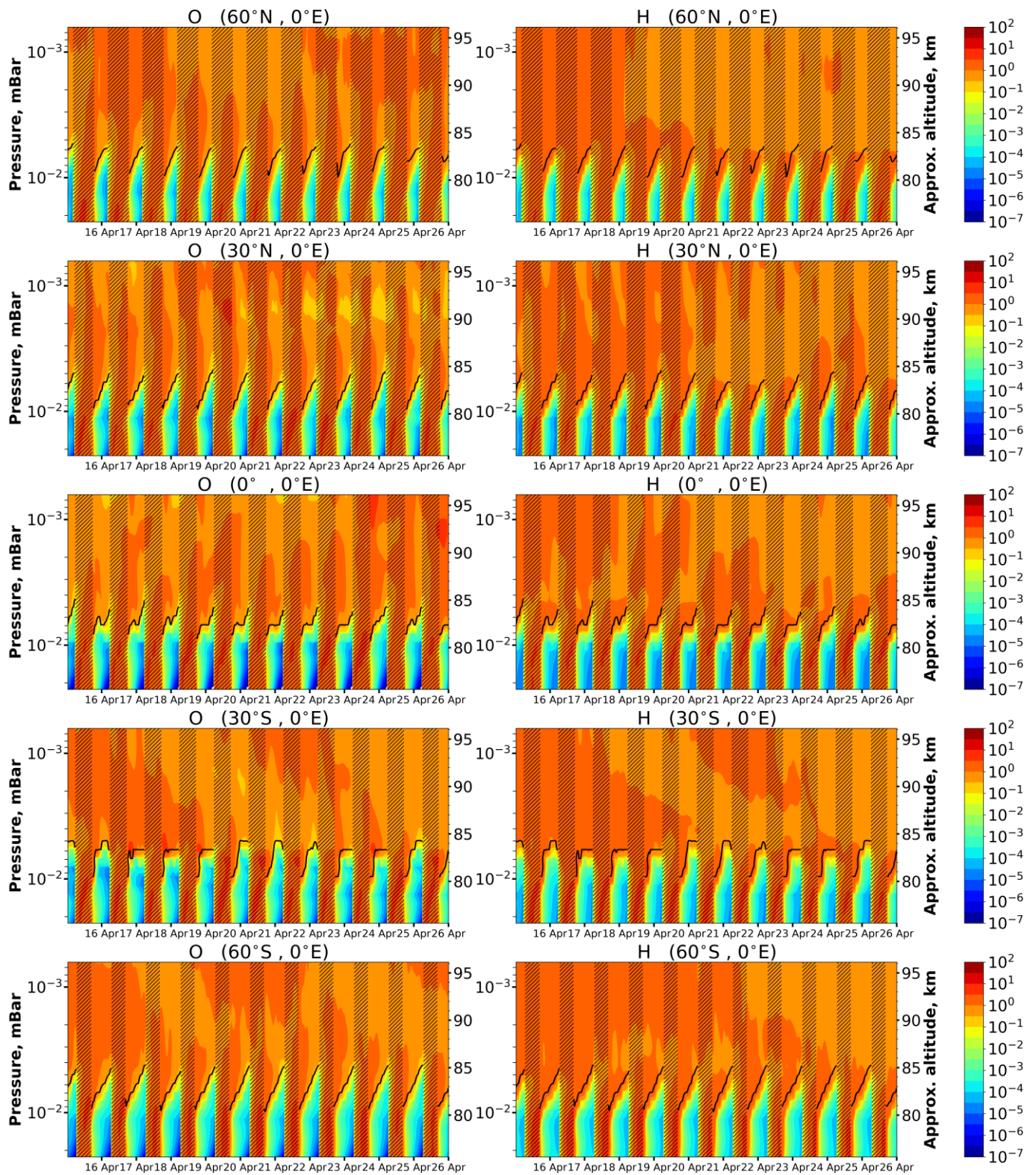
Figure 2. The same as in Fig. 1, but in April 2000. Black lines point NOCE boundary altitude according
to criterion (5) (Cr = 0.1).

636
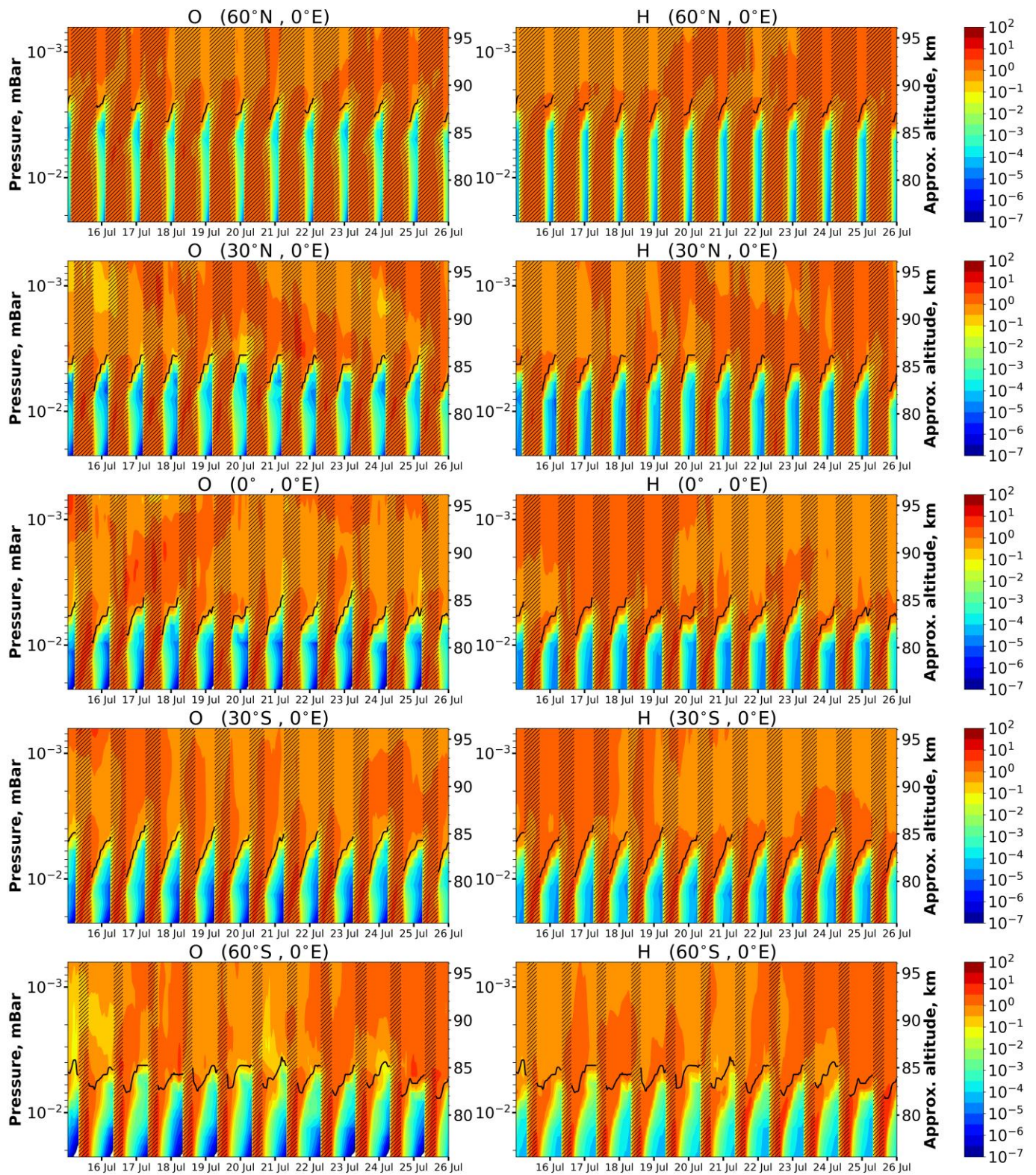
Figure 3. The same as in Fig. 1, but in July 2000. Black lines point the NOCE boundary altitude according to criterion (5) (Cr = 0.1).

641

642

643

644

645
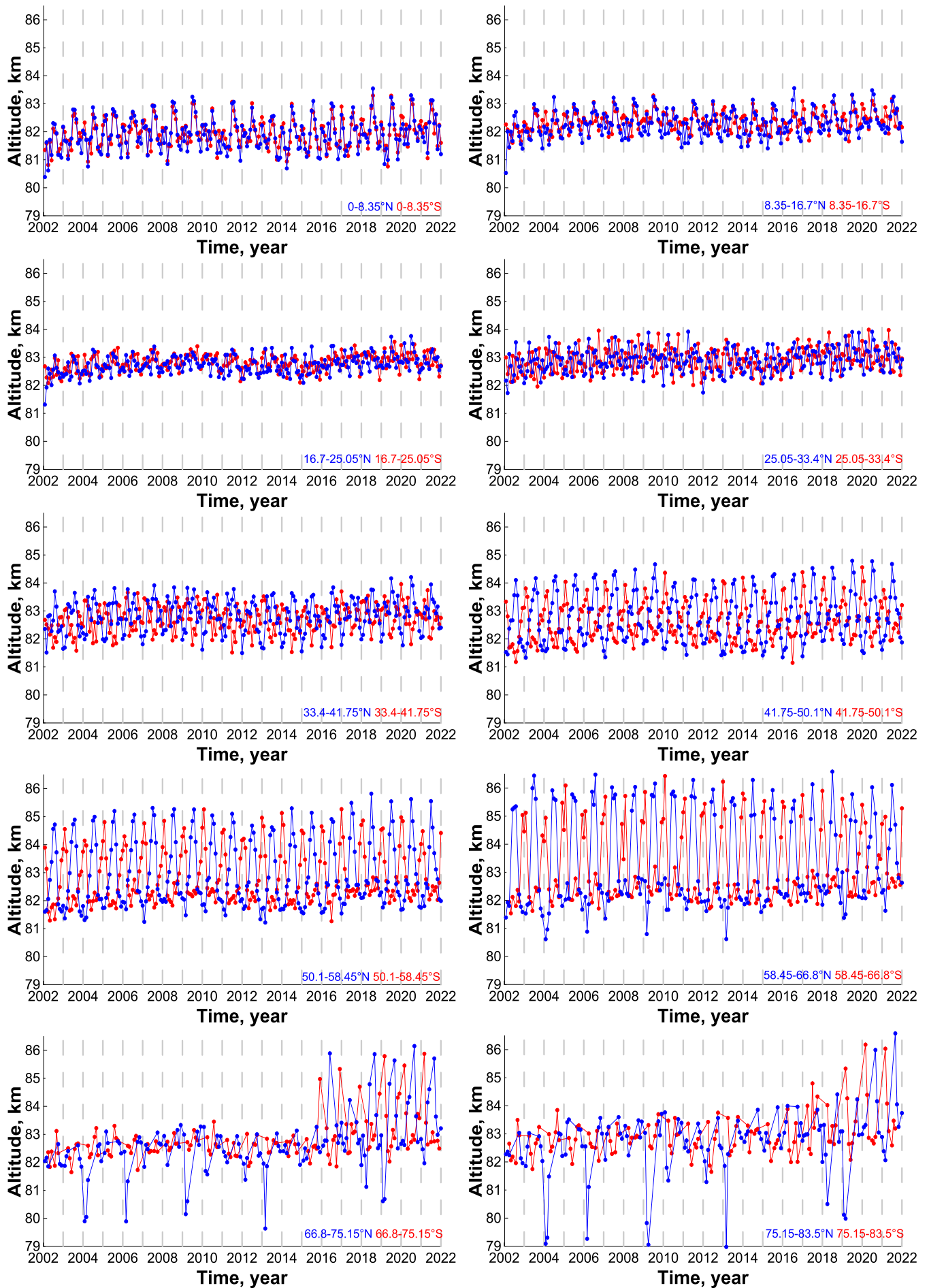
Figure 4. Time evolution of monthly mean pressure altitude $h_{eq}{}^{m}$ at different latitudes.

647
648
649
650
651
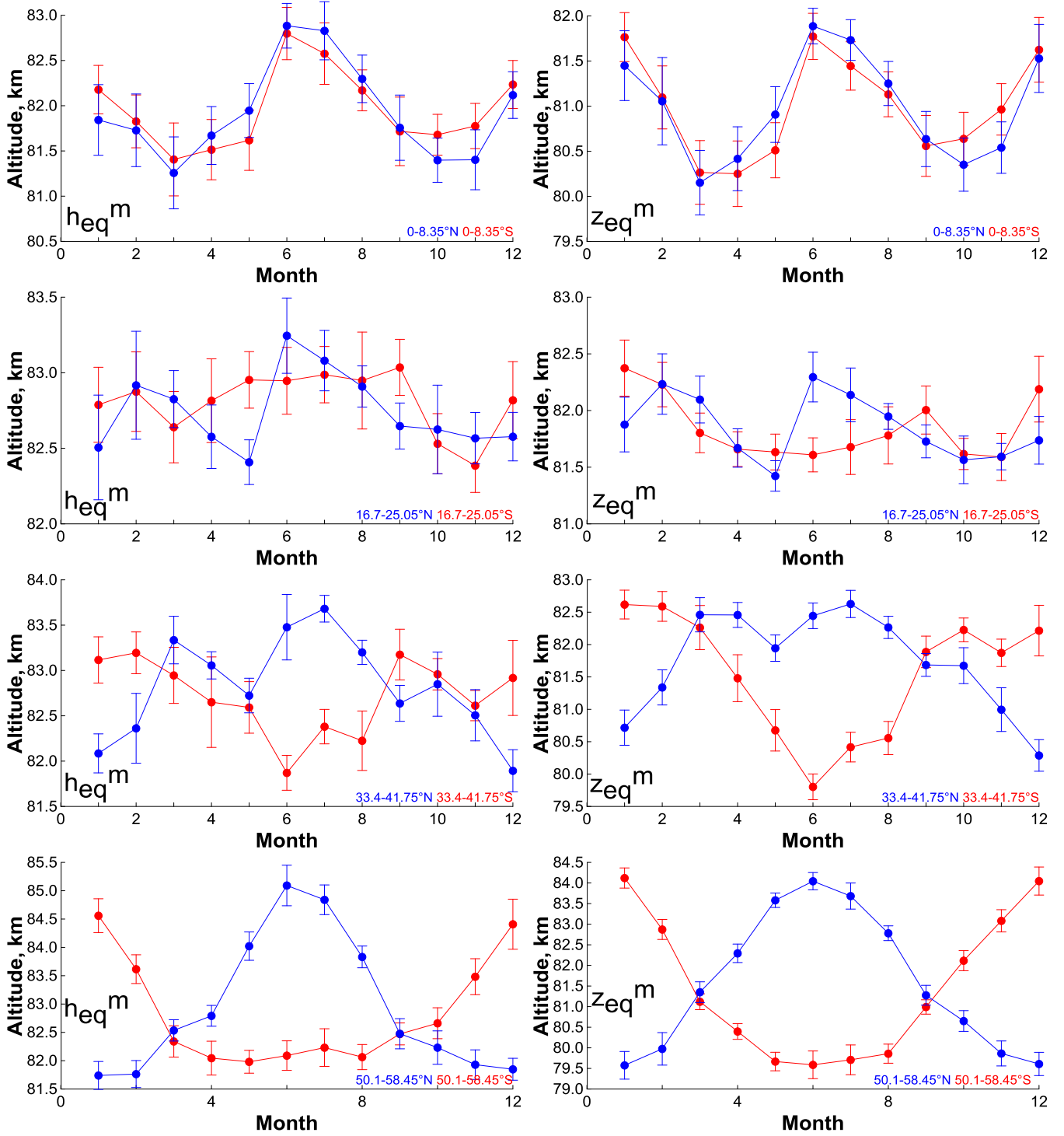
Figure 5. Average (for 2002-2021) annual cycle of monthly mean pressure altitude $h_{eq}{}^{m}$ and geometrical altitude $z_{eq}{}^{m}$ at four specific latitudes.

654

655

656

657

658

659
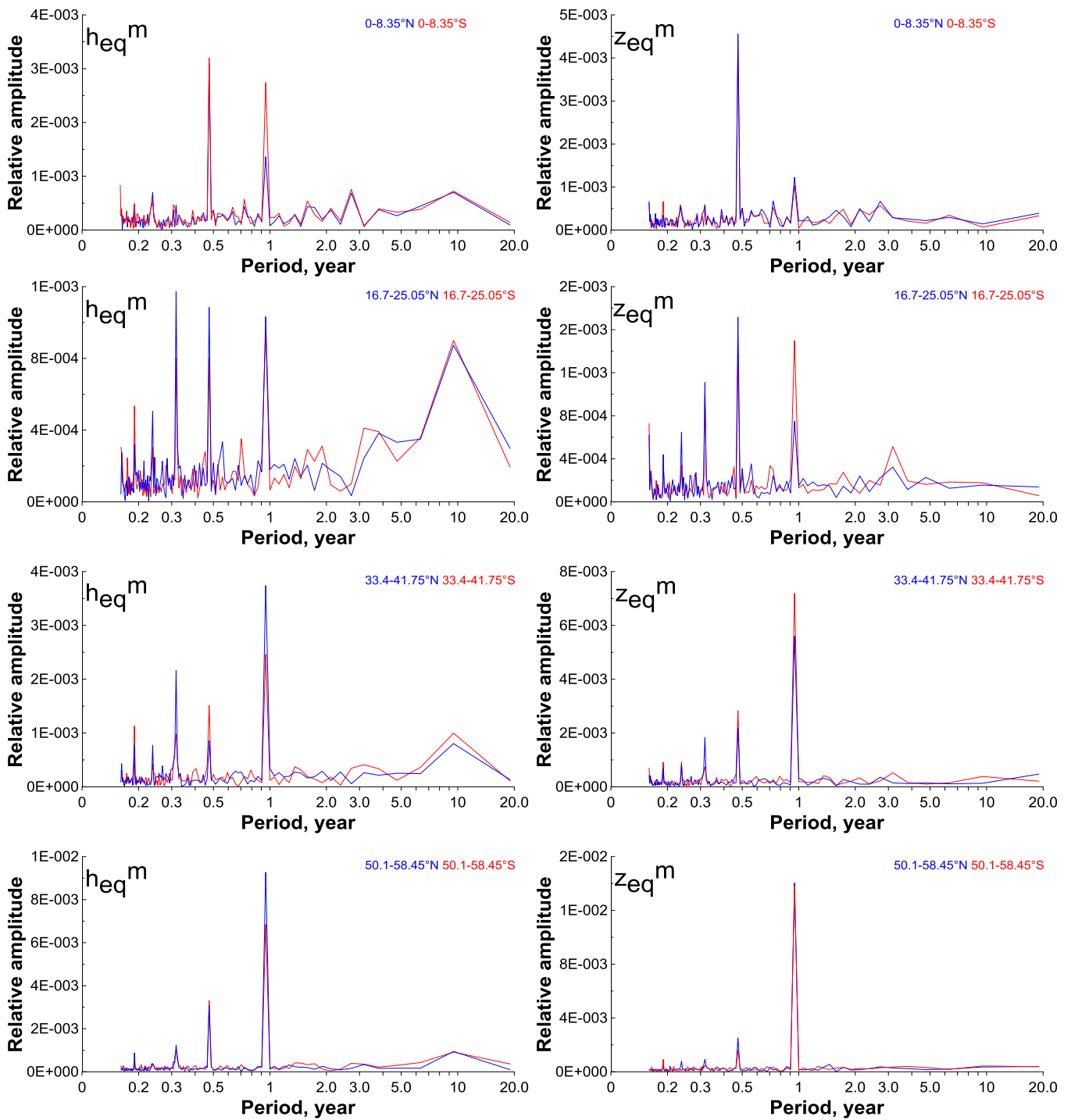
Figure 6. Fourier spectra of monthly mean pressure altitude $h_{eq}{}^{m}$ and geometrical altitude $z_{eq}{}^{m}$ at four specific latitudes. In each spectrum, the amplitudes of harmonics were normalized to the corresponding zero harmonic.

663

664
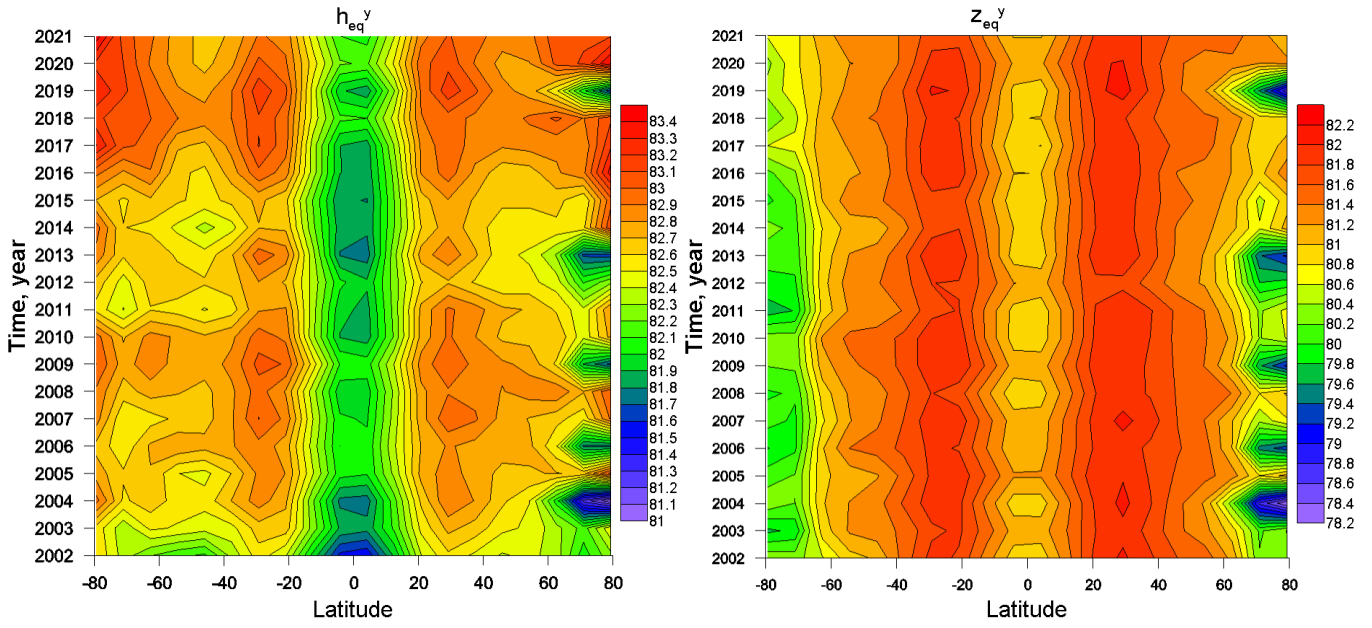
665

666 Figure 7. Latitude-time evolution of annually mean pressure altitude $h_{eq}{}^y$ (left) and geometrical altitude
667 $z_{eq}{}^y$ (right).

668
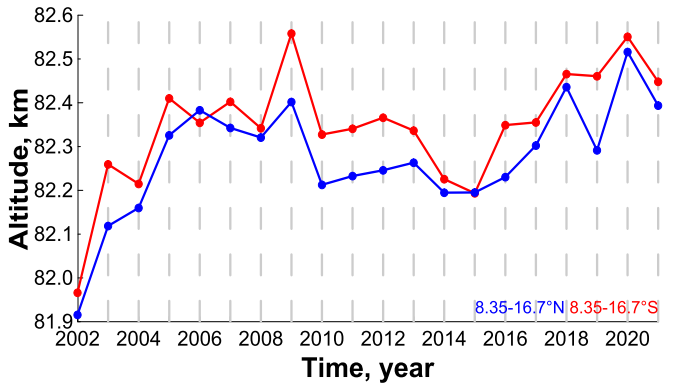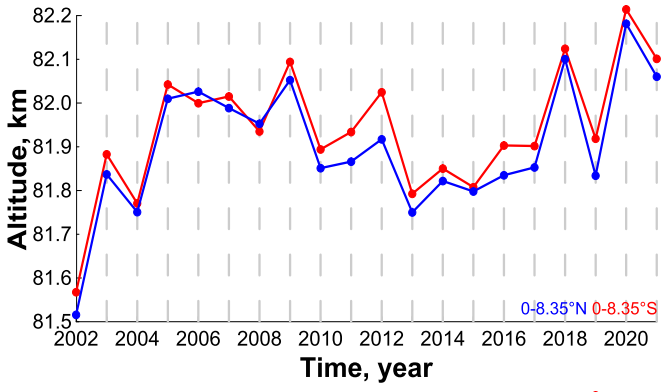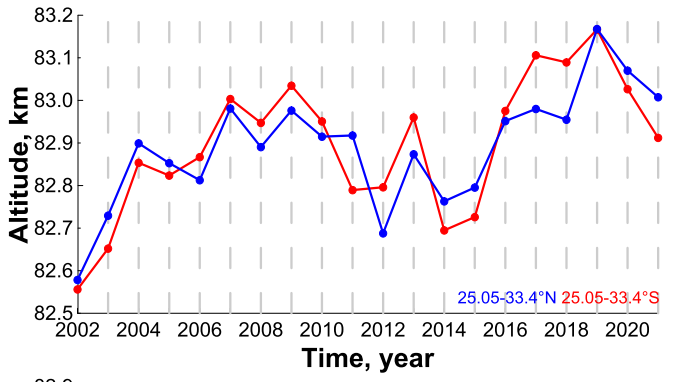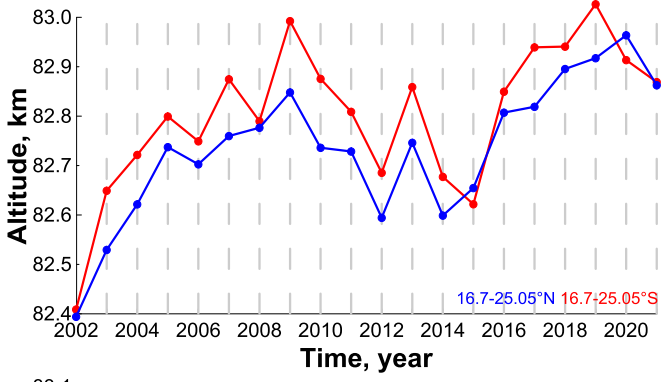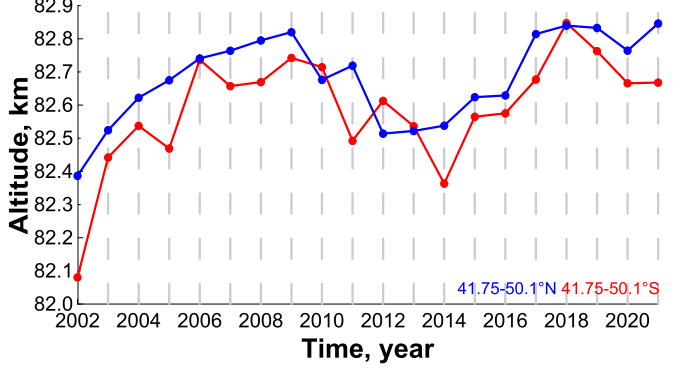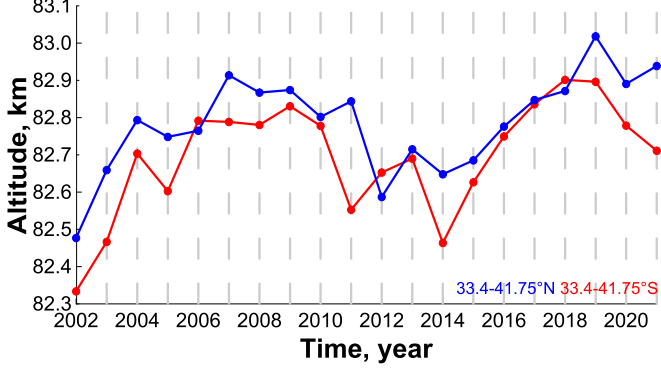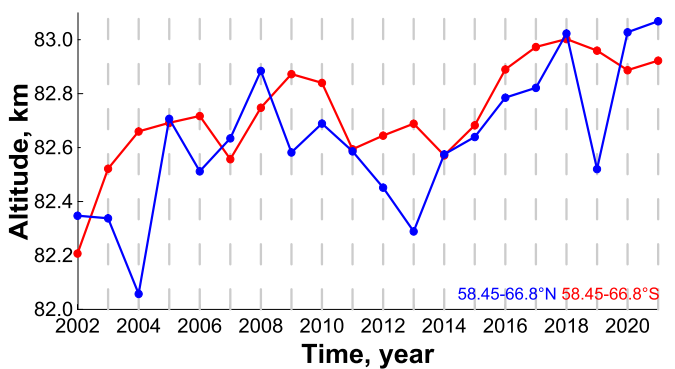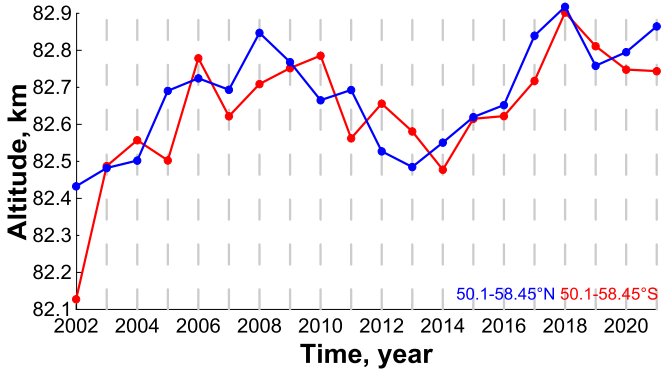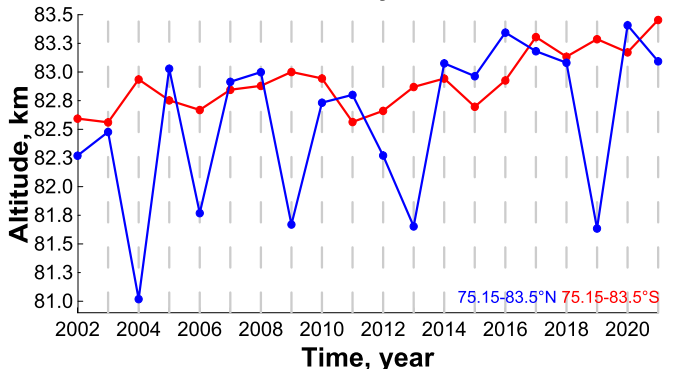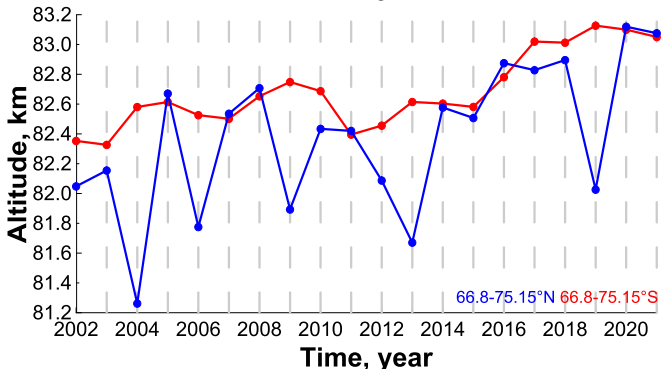
669
670
671
672
673
674 Figure 8. Time evolution of annually mean pressure altitude $h_{eq}{}^{y}$ at different latitudes.
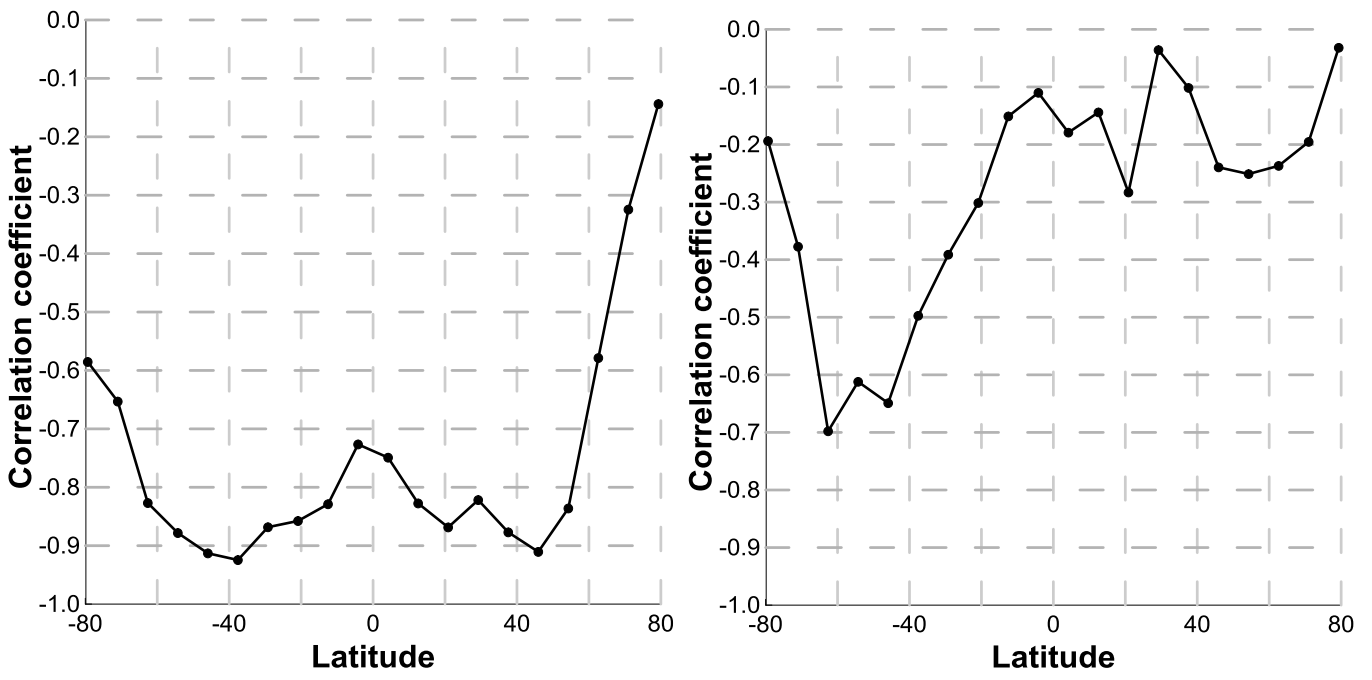
675

676 Figure 9. Correlation coefficient of $F_{10.7}$ index with pressure altitude $h_{eq}{}^{y}$ (left) and geometrical altitude

677 $z_{eq}{}^{y}$ (right) as a function of latitude.

678

679
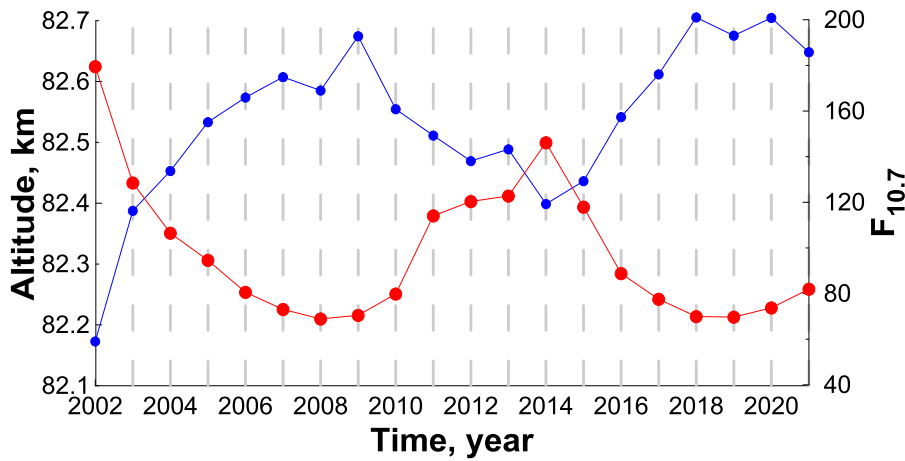
680

681

682 Figure 10. Red curve: $F_{10.7}$ index (solar radio flux at 10.7 cm). Blue curve: latitude-averaged pressure

683 altitude h_{eq}^{y} in the range between ~55ºS and ~55ºN.

684

685

686

687

688

689
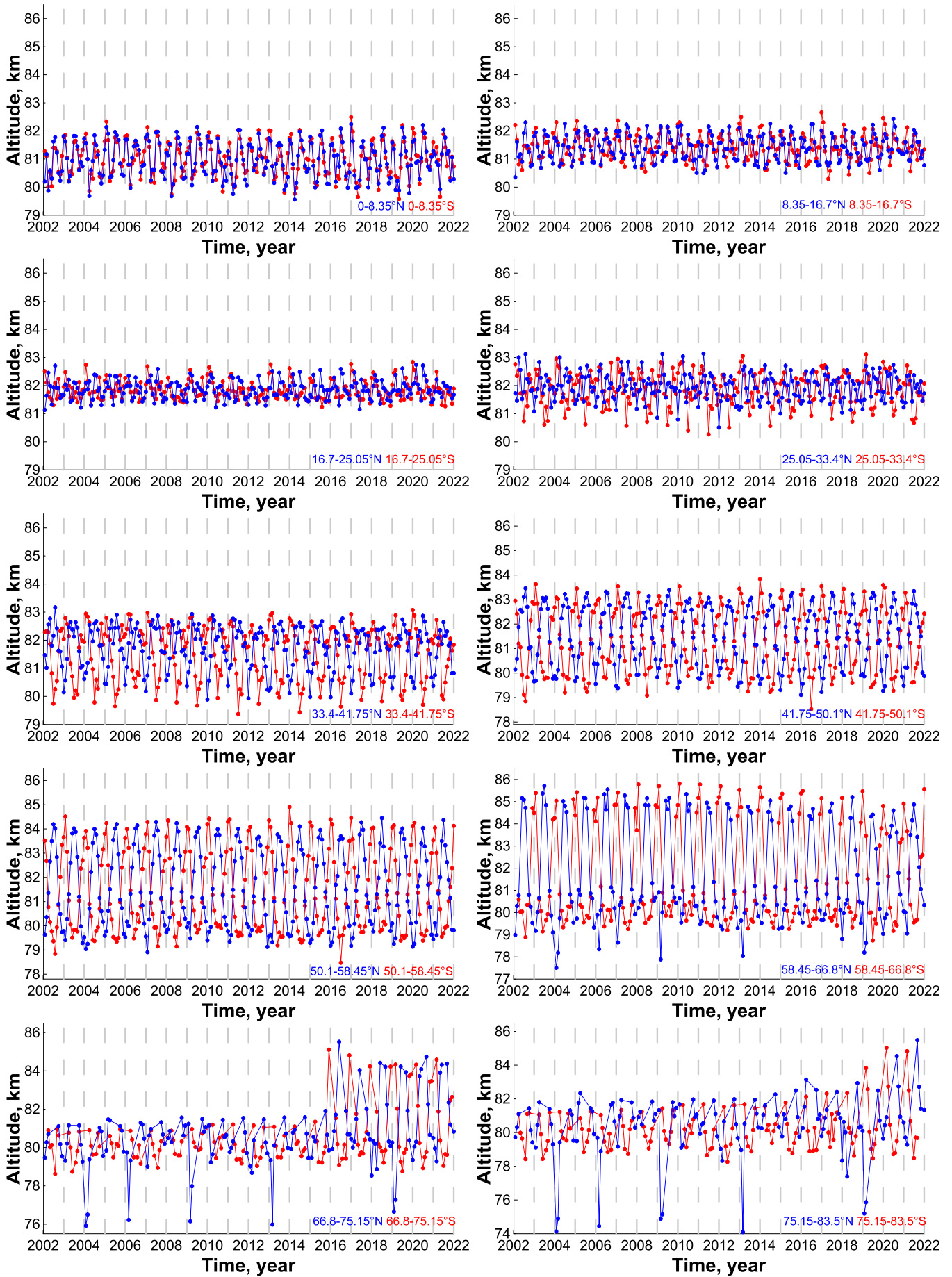
690 Figure 11. Time evolution of monthly mean geometrical altitude $z_{eq}{}^m$ at different latitudes.

691
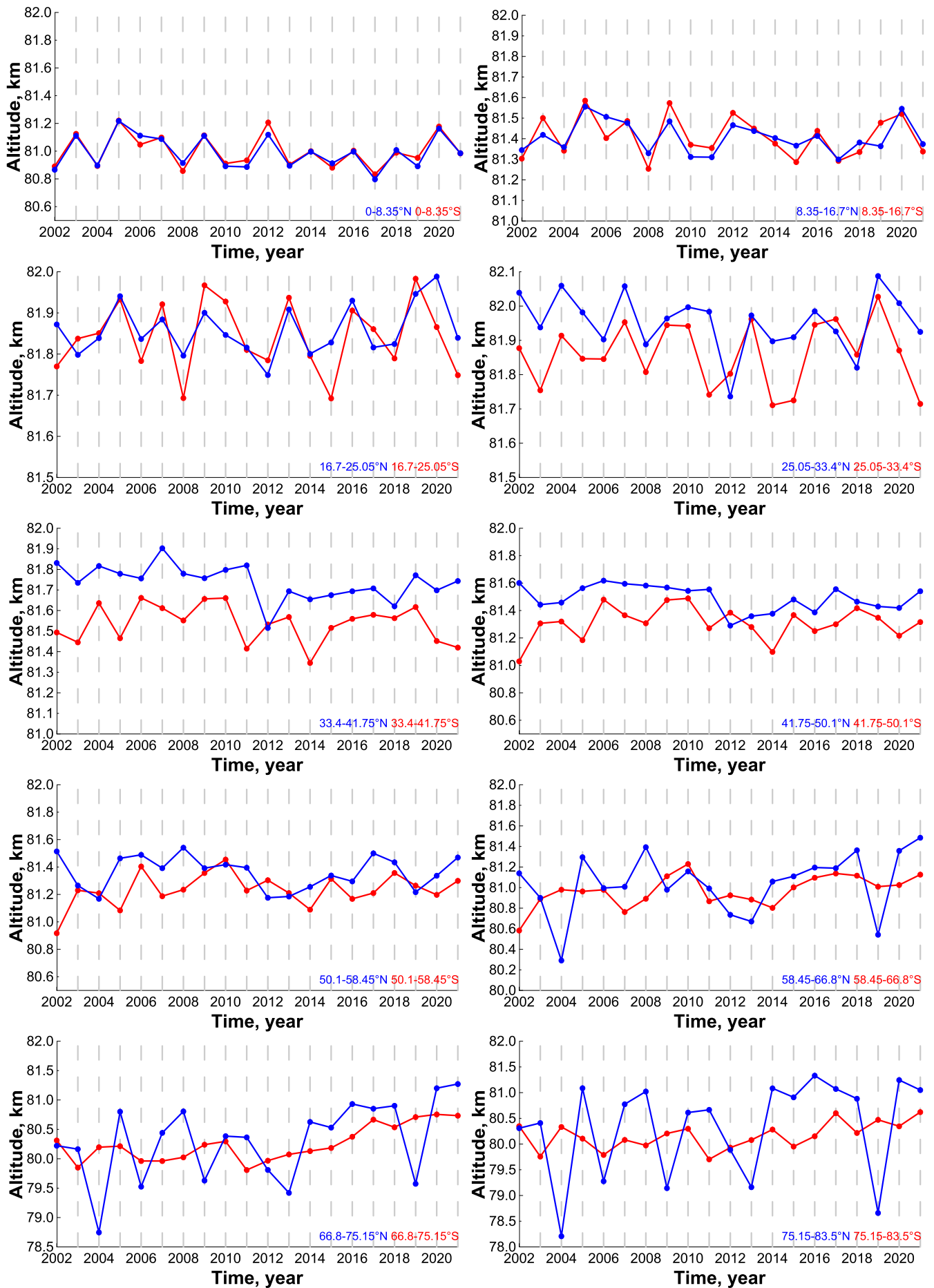
692

693

694

695

696

697 Figure 12. Time evolution of annually mean geometrical altitude $z_{eq}{}^{y}$ at different latitudes.

698
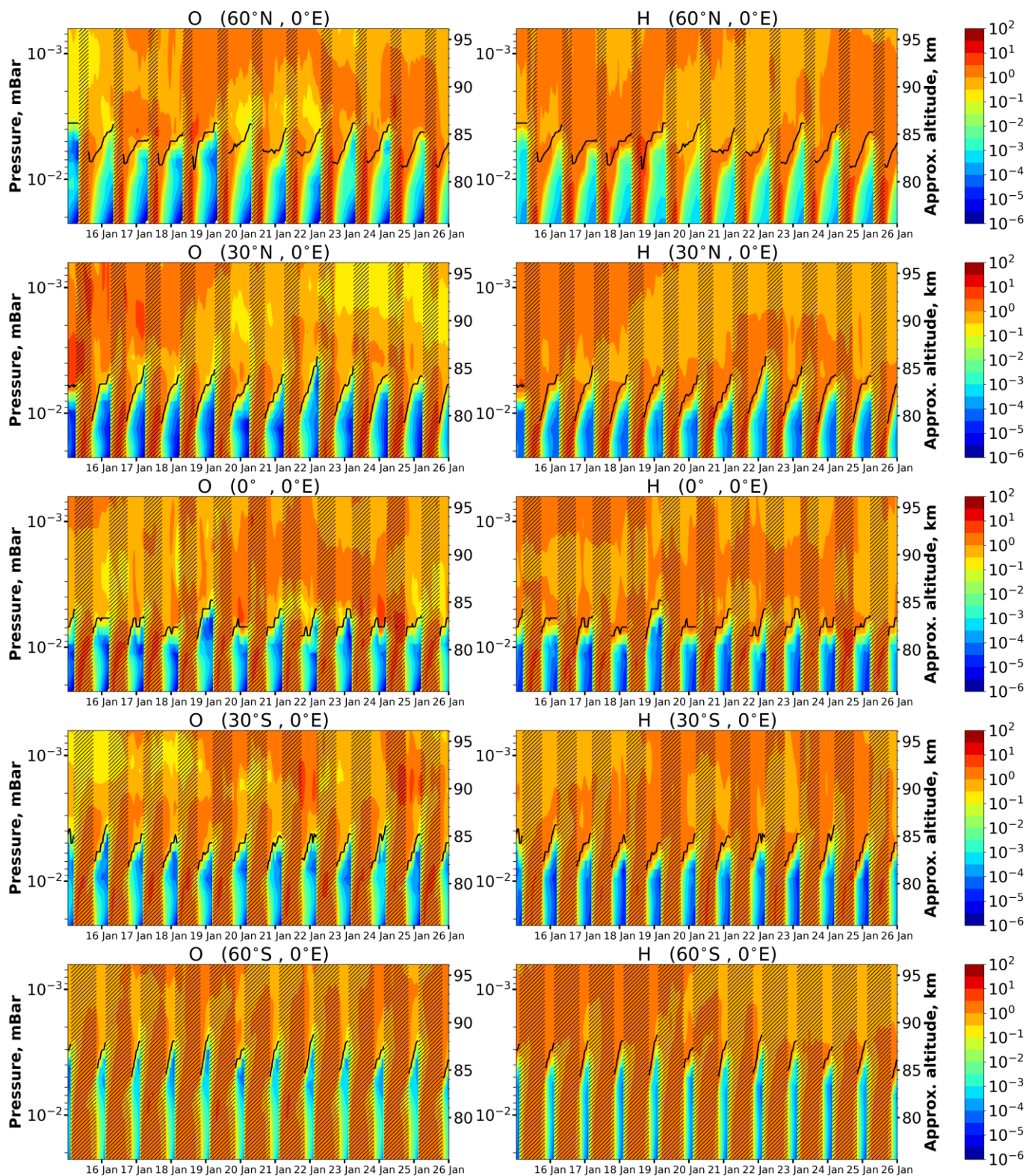
Figure 13. O and H time-height variations above different points in January 2017 calculated by 3D chemical transport model CMAM. Concentrations are normalized by mean daily values, correspondingly. Dark bars mark daytime, light bars mark nighttime. Black lines point the NOCE boundary altitude according to criterion (5) (Cr = 0.1).

703
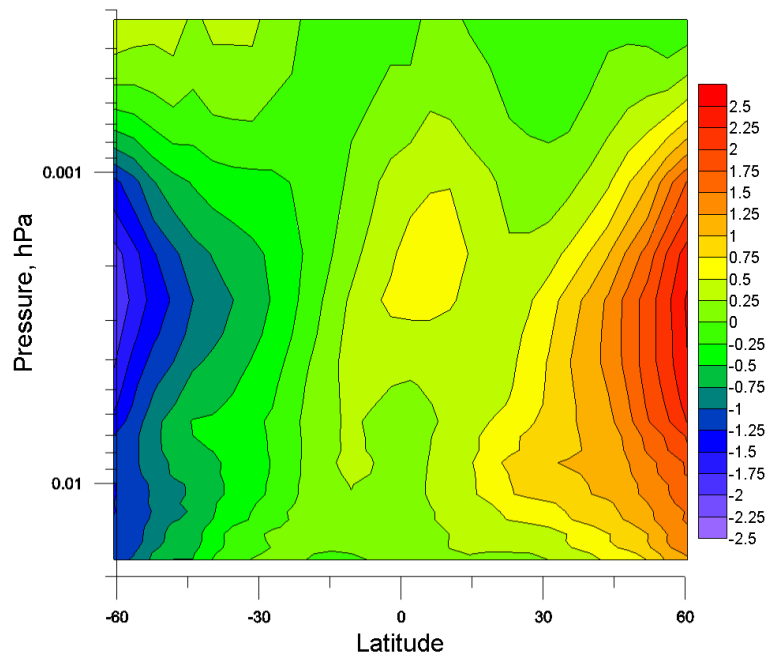
704

705 Figure 14. Logarithm of the ratio of $(O/H)_w$ and $(O/H)_s$ distributions obtained with the use of daytime
706 seasonally mean distributions of O and H averaged in 2003-2015. $(O/H)_w$ was determined from the
707 SABER data measured in December, January, and February. $(O/H)_s$ was determined from the SABER
708 data measured in June, July, and August.